8-2018

Mechanical Characterization of the Mesh-Tissue Composite Using Abdominal Wall Tissue Phantoms and Experimental Simulations

Mathew Murphy Stanford
Clemson University, mmstanf@clemson.edu

MECHANICAL CHARACTERIZATION OF THE MESH-TISSUE COMPOSITE USING ABDOMINAL WALL TISSUE PHANTOMS AND EXPERIMENTAL SIMULATIONS

A Thesis
Presented to
the Graduate School of
Clemson University

In Partial Fulfillment
of the Requirements for the Degree
Master of Science
Bioengineering

---

by
Mathew Murphy Stanford
August 2018

Accepted by:
Melinda Harman, PhD, Committee Chair
Jeremy Mercuri, PhD
B. Todd Heniford, MD

ABSTRACT

Abdominal wall hernias occur when a weakening in the muscle layer allows the protrusion of internal tissues. Hernia repair is a highly common surgical procedure with nearly one-million performed annually during which surgeons may implant surgical mesh to reinforce the weakened muscles and probe by hand to subjectively assess mesh fixation to the abdominal wall. Objective evaluation of mesh implantation relies on the mechanical characterization of the mesh-tissue composite, which is difficult in intra-operative settings. There is a need for tools capable of providing quantitative assessments of the mechanical behavior of mesh *in situ*.

While several metrics exist for characterizing soft tissues, stiffness has been shown to be a parameter relevant to clinical outcome and development of new mesh materials. A novel minimally invasive surgical tool was developed for the mechanical characterization of mesh-tissue composites in terms of their stiffness. Preliminary testing revealed variation in stiffness measurements when a load was applied to the stiffness tool by a user during operation. Through work described in this thesis, the tool was further developed with additional instrumentation to effectively minimize the impact of user-load on stiffness measurement. Characterization of the mesh-tissue composite was accomplished using commercially-available mesh, abdominal wall tissue phantoms, and a custom benchtop simulator that mimics abdominal wall distension and exposes mesh materials to biaxial loading that is comparable to physiological loading conditions.

DEDICATION

To Jennifer, Judi, and Laurie who instilled in me the importance of an education and who were a constant source of love and support through it all. I also dedicate this thesis and all of my academic achievements to my past teachers and mentors who will never know their true impact. Thank you.

ACKNOWLEDGMENTS

I would like to acknowledge my research advisor and mentor, Dr. Melinda Harman, for her dedication to this project and to my growth as an engineer. I would also like to acknowledge my committee, Dr. Jeremy Mercuri and Dr. B. Todd Heniford, MD, for their support and willingness to collaborate. Thank you to the faculty and staff of the Bioengineering Department, especially Melissa McCullough for her exceptional assistance with instrumentation. I would also like to give a big thank you to past and present members of the RE-MED lab. Thank you to Jorge Hernandez and Kyle Snethen for their support and advice, to Xinyue Lu and Moh'd Jaradat for their assistance in data collection, and to Helen Nguyen, Nicole Meilinger, and Sam Insignares for their excitement, assistance, and willingness to learn.

TABLE OF CONTENTS

Table of Contents (Continued)

Page

LIST OF TABLES

List of Tables (Continued)

Page

LIST OF FIGURES

List of Figures (Continued)

Page

List of Figures (Continued)

Page

CHAPTER ONE

PROJECT OBJECTIVE

2.1 BROAD OBJECTIVE AND SPECIFIC AIMS

The broad objective of this thesis was to characterize the mechanical behavior of the mesh-tissue composite using abdominal wall tissue phantoms and experimental simulations. This was accomplished through three specific aims presented in this thesis:

Aim 1: Develop a hand-held tool with instrumentation for mechanical characterization of the abdominal wall.

Aim 2: Characterize mesh-tissue composite stiffness in a uniaxial tension simulator with abdominal wall tissue phantoms and surgical mesh.

Aim 3: Develop a benchtop simulator to mimic abdominal wall distension and provide biaxial loading of mesh-phantom composites.

CHAPTER TWO

DEVELOPMENT OF A STIFFNESS MEASUREMENT TOOL FOR CHARACTERIZATION OF ABDOMINAL WALL TISSUE

2.1 INTRODUCTION

Herniation of the abdominal wall occurs when a weakening in the muscle layer allows internal tissues to protrude (Muyosoms 2012, Poussier 2013). Hernia repair is a common open or laparoscopic surgical procedure with nearly one-million repairs performed annually (Rutkow 1993). During the procedure, surgeons may implant surgical mesh to reinforce the weakened muscle layer and probe the mesh to subjectively assess its fixation to abdominal wall tissues (Kulaçoğlu 2015, Dabbas 2011). Relevant parameters for selection of mesh type and implantation include mechanical characterization of the mesh-tissue complex with standard uniaxial loading, biaxial loading, and *in vivo* animal models. Such test methods are limited to laboratory environments while research-grade instruments reported in literature for the mechanical characterization of biological tissue are incompatible for use *in situ* due to excessive size and other incompatibilities with intra-operative settings. (Li 2012, Ottensmeyer 2001, Samur 2007).

Several metrics exist for defining the mechanical characteristics of soft tissues, including tensile, compressive, and shear strength. Among these, stiffness is of considerable interest for abdominal wall research and hernia repair (Li, J). A novel minimally invasive surgical tool was developed for the mechanical characterization of the mesh-tissue composite with intended application to hernia repair surgery. Under simple

tension or compression, the force response of these tissues can be described as having an initial exponential region followed by a linear elastic region. The prototype stiffness tool used an instrumented probe with force and displacement sensors to indent the mesh-tissue composite for mechanical characterization in terms of stiffness (N/mm) extrapolated from the slope of the linear region.

Preliminary testing with the stiffness tool revealed variation in stiffness measurements when a load was applied to the tool by a user during operation (Hernandez 2016). To normalize stiffness measurements and remove the effects of increased load on the tool, an additional sensor was required to quantify the load magnitude – referred to in this thesis as "user-load." Experimental procedures for further development of the prototype stiffness tool outline in Figure 2.1 included 1) incorporation of additional instrumentation, 2) calibration of three sensors within the tool, 3) verification of measurement accuracy and repeatability, and 4) verification with tissue phantoms and animal models.

2.2 METHODS

Prototype Design

Design inputs for the stiffness measurement tool were derived from methods of spherical indentation which require 1) a semi-infinite model in which the sample plane extends perpendicular to the axis of indentation with a large depth of material beneath, 2) a ratio of a spherical indenter tip diameter to sample diameter less than or equal to 1:10, and 3) a ratio of indentation depth to spherical indenter diameter to be less than or equal

to one (Ottensmeyer 2001, Chhetri 2011, Pawlak 2003). To meet these requirements, the tool was designed with three main functional sections: the body and handle, indenter rod and reference ring, and the actuation mechanism.

The body casing of the hand-held stiffness tool was designed to have an ergonomic pistol-grip shape commonly used in surgical tools with an outlet through the rear face to bundle instrumentation cables extending from internal sensors. The tool casing was created using additive manufacturing for rapid prototyping and iterative design. The indenter consists of a brass rod and attached 10 mm diameter spherical indenter. In ball-burst mechanical testing, a clamp assembly functions as a limiting reference plane for an indented mesh sample. Such an assembly is not applicable *in vivo* or *in situ*. To mitigate effects of motion artifacts during indentation, a 3D-printed cone-shaped reference ring with 20 mm diameter was designed at the distal end of a sheath rigidly attached to the body of the stiffness tool and concentric to the indenter rod. The indenter rod was designed to be linearly driven by an actuation mechanism within the casing (Figure 2.2).

Internally, the casing has rails which guide linear actuation of the indenter and hard stops to limit indenter displacement to 10 mm. The actuation mechanism is a system of gears, rack and pinion, and a trigger which drive a carriage along parallel rails. The carriage houses an indenter force sensor in-line with the attached indenter rod, as well as a reflective target. As the target displaces with the carriage, a displacement sensor detects the change in position. These indenter sensors output analog voltage values to be interpreted by an Arduino UNO board (Arduino, USA) for conversion to units of force

(N) and displacement (mm) through scripts written in MATLAB (MATLAB R2017a, Math Works, USA).

Incorporating a User-Load Sensor

Accurate measurement of user-load applied to the stiffness tool required redesign to accommodate a new force sensor while also allowing full functionality of existing instrumentation. Considerations for an appropriate user-load sensor included flexible strain gauges, beam-shaped load sensors, and a through-hole “donut” load sensor. Ultimately, a through-hole load sensor was chosen to detect changes in user-load applied to the stiffness tool.

Preliminary tests found that a 4 lbf (18 N) load was sufficient force to maintain contact between the sheath and an indented sample at full indentation; thereby also identifying the required minimum force capacity of a user load sensor. The through-hole “donut” type load cell (LC8100-200-10, OMEGA, Stamford, CT) was selected with a maximum capacity of 10 lbf (44 N) compressive load (Appendix C). This could easily accommodate the required force while also allowing a margin of safety for increased load. The "donut" type design – having a 5.1 mm inner and 25.4 mm outer diameter – allows the force sensor to sit in-line and concentric with the indenter rod.

The internal structure of the stiffness tool’s body was modified to house and support the additional sensor (Figure 2.3). This was accomplished by designing a cage structure within the front section of the tool, just behind the sheath. A plate of 5 mm thickness extruded in both halves of the case serves as a support for the user-load sensor

in addition to four cylindrical pins extending perpendicular from the plate to the front of the case. With casing halves together, the pins are equally spaced apart at a diameter equal to the sensor. Together, the pins and plate function to hold the sensor concentric with the indenter rod and sheath while a hole in the plate allows sensor wires to be threaded through the casing body (Appendix B). Multiple design iterations of the front section were rendered in SolidWorks CAD software (SolidWorks 2017, Dassault Systemes, France) and 3D printed into prototypes with changes made as needed.

The sheath was modified for axial transfer of load to the user-load sensor. Locking flanges and grooves were removed from the sheath and front of the casing as previously designed to allow the sheath to rotate and displace freely. In the current design, double female threads were cut along the internal surface of the sheath to 5 mm with a 10 mm pitch opposite the reference ring. A small washer 25 mm in diameter and 1.25 mm thick was also designed and 3D printed to sit between the user-load sensor and front wall of the tool's casing. Male threads complementary to those in the sheath were extruded from one side of the washer (Appendix B). With this design, the sheath could be easily removed and threaded onto the washer in a half-turn to sit in-line with the user-load sensor and concentric with the indenter rod.

In addition to functional design alterations to accommodate a user-load sensor, cosmetic changes were made to the stiffness tool for ease of assembly. Previously, the casing halves were fixed with screws. The tool design was altered to incorporate a 3D printed clamp which wraps around the handle, sitting flush with the case surface. Additionally, a threaded ring was 3D printed to screw onto the front face of the tool,

concentric with the sheath, thereby clamping the two casing halves together. The outlet for sensor wires was moved to the bottom of the tool's handle to keep wires from interfering with the user's hand.

Calibration of Instrument Sensors

The load and displacement sensors previously described required calibration within the redesigned stiffness tool and comparison to a calibrated benchtop mechanical testing system to ensure accurate measurements. Calibration of each sensor required loading conditions which mimic those expected during application of the tool. The user-load sensor, for example, was calibrated under tension by the manufacturer but application in the tool required compressive loading. The displacement sensor maintains high sensitivity to the position of the reflective target relative to the LED component and was calibrated accordingly.

The user load sensor was calibrated by fixing the stiffness tool in a rigid clamp stand with the indenter directed upward. The removable sheath and threaded washer were assembled in the tool, making contact with the sensor. Eight combinations of small weights ranging from zero to 2.8 kg (0-6 lb.) were placed on the reference ring at the distal end of the sheath. Weight masses were converted to force in Newtons and recorded with the voltage output at each weight increment. A force versus voltage calibration curve was created for the user load sensor.

Similarly, the indenter load sensor was calibrated by rigidly fixing the stiffness tool in a clamp stand with the indenter directed upward. The indenter rod was fully extended

while the indenter tip and sheath were removed to expose the rod for ease of placing calibration weights. Six combinations of small weights ranging from zero to 1.5 kg (0-3 lb.) were placed on the distal end of the rod (Figure 2.4). Weight masses were converted to force in Newtons and recorded with the voltage output at each weight increment. A force versus voltage calibration curve was created for the user load sensor.

The displacement sensor was calibrated by fixing the tool in a rigid clamp stand with the indenter directed downward (Figure 2.5). The sheath and indenter tip were removed for ease of use with a calibration gauge. A digital dial indicator (0.01 mm resolution, Series 543 Absolute Digimatic Height Gage, Mitutoyo Corporation, Sakado, Japan) was rigidly fixed below and placed in contact with the indenter rod at which the gauge origin position was set. The tool's trigger was progressively squeezed and held with a small clamp, effectively protruding the indenter rod and displacing the internal reflective target. Twenty measurements were obtained by incrementing indenter rod displacement between full retraction and full protrusion positions of the indenter. Displacement measurements in millimeters and corresponding voltage output were recorded at each increment. A displacement versus voltage calibration curve was created for the displacement sensor.

Linear regression was performed on the force and displacement versus voltage curves for each sensor to ensure accurate measurements. Linear models for each unit of measure (y) as a function of voltage output (x) were defined and R^2 values were used to evaluate linearity.

Verification of Measurement Accuracy and Repeatability

The accuracy and repeatability of measurements acquired with the stiffness tool were verified through comparison with measurements acquired by a bench-top mechanical testing system (ElectroForce 3200, BOSE Corporation, Massachusetts, USA). Accuracy was defined by the absolute difference between measurements acquired by the BOSE and those by the stiffness tool. Repeatability was defined as the absolute difference between measurements acquired by the same instrument. To directly compare the two measurement instruments, a spherical indenter identical to that of the stiffness tool was fabricated and directly attached to the force sensor and moving piston of the BOSE ElectroForce system.

For verification of the indentation load and displacement sensors, a spring assembly was characterized in terms of stiffness. A spring, 9.5 mm in diameter and 33 mm in length, was fixed at one end within a small cylindrical enclosure. A conical tip attached to the free end was used to guide and center the stiffness tool and BOSE system indenters on the spring (Figure 2.6). During testing with the tool, the reference ring was fixed against the spring assembly and the trigger was pulled to compress the spring five times at a constant rate of 10 mm/s. The BOSE system indenter was set to the same displacement rate and starting position on the spring assembly for five compression tests. Spring stiffness values were extrapolated as the slope of force-displacement curves through linear regression analysis.

Verification of the user load sensor was accomplished by applying a weight of known mass to the BOSE system and stiffness tool similar to calibration methods. The

tool was fixed in a rigid clamp stand with the indenter directed upward. A 900 gram (8.82 N) weight was placed on the distal end of the sheath five times and force data was collected through MATLAB. During testing with the BOSE ElectroForce, the system's force sensor was attached to a rigid platform and a small stage was attached atop the sensor (Figure 2.7). The system was programmed with Wintest 7 software (BOSE Corporation, Massachusetts, USA) to negate the force applied by the stage and to output force data acquired under the weight load. Force measurements were repeated five times.

Stiffness and load measurements acquired with the BOSE system and stiffness tool were compared statistically using a Student's *t* test. All statistical tests were performed using Minitab software (Minitab 18, Minitab Inc., State College, USA).

Verification with Tissue Phantoms

Simulation of the abdominal wall required materials that mimic physiological stiffness. Verification of the hand-held stiffness tool could then be performed with application to such tissue phantom materials. To simulate the abdominal wall, it was necessary to first consider its elastic modulus (E), which is reported to be 20 to 50 kPa (Song 2006a, Song 2006b). A corresponding abdominal stiffness range of 0.33 to 0.81 N/mm was extrapolated from a force-displacement curve (Figure 2.8) created using Equation 1 to describe the force response of incompressible tissues under spherical indentation:

$$F = \frac{4}{3}\frac{E}{1-\nu^2}\, d^{\frac{3}{2}} R^{\frac{1}{2}} \quad \text{(N)} \qquad \text{[Equation 1]}$$

where the Poisson ratio, ν, equals 0.5, indenter radius, R, equals 5 mm, and indentation depth, d, ranges from 0 to 10 mm (McKee 2011).

Synthetic tissue phantoms were created using commercially available silicone rubber having elastic moduli within the range of abdominal wall stiffness values (ECOFLEX, Smooth-On, Texas, USA). Two shore hardness formulations, OO-10 and OO-20, were chosen with theoretical elastic moduli bracketing physiological values of 41 kPa and 60 kPa, respectively (Pawlak 2003). Silicone gels of each modulus were cast in plastic containers, creating cylindrical phantom samples 83 mm in diameter and 76 mm in height (Figure 2.9).

The mechanical behavior of the tissue phantoms was first characterized with the Bose ElectroForce mechanical testing system (ElectroForce 3200, BOSE Corporation, MA, USA). In accordance with the requirements for spherical indentation, the ElectroForce was fitted with a 10 mm-diameter spherical indenter tip attached to the system load cell and vertical actuator. A tissue phantom of each modulus formulation was centered beneath the indenter and probed five times to a depth of 10 mm at a rate of 10 mm/s (Figure 2.10). The reaction force and indenter displacement data from all testing was recorded to create force-displacement curves for each indentation. The stiffness of each phantom was calculated as the slope of the linear region evident in the range from 5 to 10 mm of indentation.

Tissue phantoms were then characterized by the stiffness measurement tool. This was achieved by rigidly fixing the tool within the Instron hydraulic mechanical testing frame (model 5944, Instron, Norwood, MA, USA). The tool was attached to the system's

50 N load cell and displacement actuator for precise control of load applied to the tool (Figure 2.11). During testing, each tissue phantom was centered beneath the indenter tip and the tool was lowered to make contact between the reference ring and phantom's surface. Each tissue phantom was probed under two user-load conditions:

1. Without user-load, in which the reference ring was held at the surface of the phantom without displacing into the sample
2. With user-load, in which the Instron was programmed (Bluehill Software, Instron, USA) to lower the stiffness tool until a 10 N load was applied at which point the tool was held rigid throughout indentation

Under each condition, phantoms were subjected to five repetitions of indentation to a depth of 10 mm at a rate of 10 mm/s. Stiffness values were then extracted from the linear region of the force-displacement curve. Statistical analysis was accomplished in three phases:

1. Mean stiffness values of the two phantom formulations measured by the BOSE were compared statistically using *t* tests to confirm phantom stiffness is representative of physiological stiffness.
2. Mean stiffness values obtained on the same phantom formulation with no user-load in the bench-top BOSE and stiffness tool measurement systems were compared using a paired *t* test.
3. Mean stiffness values measured by the tool under no load and with an applied user-load for each phantom were compared using a paired *t* test.

In Vivo Verification in Animal Model

For further verification of the stiffness measurement tool, a protocol was developed for experimental application of the tool to swine cadaver specimens in an *in situ* setting. Two young female swine, weighing approximately 40 kg each, were obtained after open and laparoscopic surgery of the abdomen with incision along the midline. Within one hour prior to testing, each specimen was euthanized and sutured to close the abdominal wall. The cadavers were labeled A and B with a grid of 18 measurement points identified across each abdomen for indentation. Measurement points were spaced evenly and mirrored across the sagittal plane with 10 placed along the medial line and 8 laterally. Skin and fat layers of the abdomen were resected back to expose the underlying rectus abdominis and external oblique muscles (Figure 2.12).

The stiffness tool was applied to probe both specimens five times at each measurement point (Figure 2.13). Each point was probed with minimal user-load during which the reference ring was placed just in contact with the tissue and held rigid during use to minimize load applied to the tool. Testing was then repeated with a high increase in user-load applied to the tool. The stiffness values extrapolated from force-displacement curves from each indentation were then collected to map the stiffness of each specimen's abdominal wall. Stiffness measurements acquired with Low and High user-load conditions were compared to determine a relationship between user-load and change in stiffness. The effect of user-load (Low and High) on measured stiffness was evaluated using paired *t* tests to compare mean stiffness values measured by the tool under each load condition at points 8 and 18 of both specimens.

2.3 RESULTS

Design and Incorporation of a User-Load Sensor

The stiffness measurement tool was successfully redesigned with emphasis on incorporating a user-load sensor and allowing full-functionality of existing instrumentation. Through iterative design and rapid prototyping, the final prototype design included significant modifications to the indenter sheath and casing body to accommodate a user-load sensor. Design inputs and corresponding outputs derived from requirements of spherical indentation and user-load evaluation are presented in Appendix A, Table A-1.

Calibration of Instrument Sensors

The user-load, indenter load, and indenter displacement sensors all showed a linear behavior ($R^2 > 0.9$). Therefore, simple linear models were adequate for conversion of voltage values to corresponding measurement units (Figure 2.14). These models were incorporated into MATLAB scripts for processing raw voltage outputs by each sensor and acquired by the Arduino board. Force (N) and displacement (mm) calculated as functions of voltage were used to plot force versus displacement and user-load versus time.

Verification of Measurement Accuracy and Repeatability

Characterization of the spring assembly with the BOSE system and hand-held stiffness tool found the spring to have a stiffness of 2.19±0.89 N/mm and 2.47±0.30

N/mm respectively. This showed a 12% difference between the mean stiffness measurements and high accuracy of the stiffness tool, with no statistical difference between mean stiffness measurements (Student's *t* test, p=0.106). Additionally, the weight load applied to the BOSE system was measured at 8.90±0.01 N, while the stiffness tool measured the load at 8.74±1.04 N, showing 1.8% difference in load measurement and high accuracy of the user-load sensor. There was no statistical difference between the mean load measurements (Student's *t* test, p=0.746). Additionally, standard deviations of stiffness and user-load measurements by the stiffness tool were equivalent to 12% and 11% variations respectively, showing acceptable precision.

Verification with Tissue Phantoms

Tissue phantoms were successfully characterized in terms of stiffness from indentation tests with the BOSE ElectroForce system and stiffness measurement tool. Stiffness values were extrapolated from the linear region of each force-displacement curve through linear regression in the range from 5 to 10 mm of indentation. A linear relationship was observed with $R^2>0.9$ for all measurements.

Statistical analysis revealed a significant difference ($p<0.001$) between mean stiffness values of the OO-10 and OO-20 phantom formulations measured by the BOSE ElectroForce at 0.599±0.001 and 0.709±0.001 N/mm respectively. Therefore, the abdominal wall tissue phantoms were considered different from one another and within the physiological range (0.33-0.81 N/mm). No significant difference ($p>0.05$) was found between mean stiffness measurements obtained by the BOSE and stiffness tool on the

same tissue phantom sample (Figure 2.15). A difference of 6.5% was observed between mean stiffness measurements acquired by the BOSE and tool on both tissue phantoms, again showing high accuracy of the stiffness tool. Statistical analysis also showed mean stiffness values measured by the tool under different user-load conditions on the same phantom to be statistically different from one another ($p<0.05$), confirming that an increase in applied load can cause a significant increase in measured stiffness (Figure 2.16).

In Vivo Verification in an Animal Model

The abdominal wall of both swine cadaver specimens was successfully mapped and characterized in terms of stiffness by probing with the stiffness measurement tool. Stiffness values obtained at all measurement points were extrapolated from the linear region of each force-displacement curve through linear regression in the range from 5 to 10 mm of indentation (Figure 2.17). A linear fit was observed with $R^2>0.9$ for all measurements.

All stiffness measurements acquired with a High applied load to the tool were greater than those with a Low load (Table 2.1). Analysis revealed a significant difference between stiffness values measured under a Low applied user-load and those under High load on the same measurement point ($p<0.05$) except for point 8 on specimen A ($p=0.975$) (Figure 2.18). This again confirms that user-load applied to the tool during indentation can significantly increase stiffness measurements.

2.4 CONCLUSIONS

A hand-held stiffness measurement tool was developed with the capability of characterizing abdominal wall tissue phantoms and measuring user-load applied to the tool thereby satisfying Aim 1 of this thesis. A user-load sensor was successfully implemented through iterative design of the stiffness tool and instrumentation verification. A small "step" seen in the lower range of forces in the calibration curve was interpreted to indicate a lower limit of 5 N for accurate measurement of user-load applied to the stiffness tool.

Abdominal wall tissue phantoms cast from silicone rubber were characterized in terms of stiffness with magnitudes falling within the range of physiological stiffness as measured by the tool and standard benchtop equipment. Measurements acquired with the stiffness tool were comparable (within 6.5%) to those measured with the ElectroForce system, thereby highlighting the tool's relatively high accuracy for a hand-held prototype instrument. An experimental protocol was designed to study the relationship between user-load applied to the tool and measured stiffness. Testing on tissue phantoms and animal models revealed that load applied to the hand-held stiffness tool during indentation can significantly increase the measured stiffness and that the tool can distinguish variations in stiffness due to user-load. Therefore, accurate measurement of user-load is necessary to correct for variability in stiffness measurements caused by the applied load. Based on these positive results, a more robust tissue phantom model and experimental design with surgically relevant mesh material was pursued (Specific Aim 2)

to better simulate *in situ* conditions and evaluate the effects of user-load on stiffness measurement.

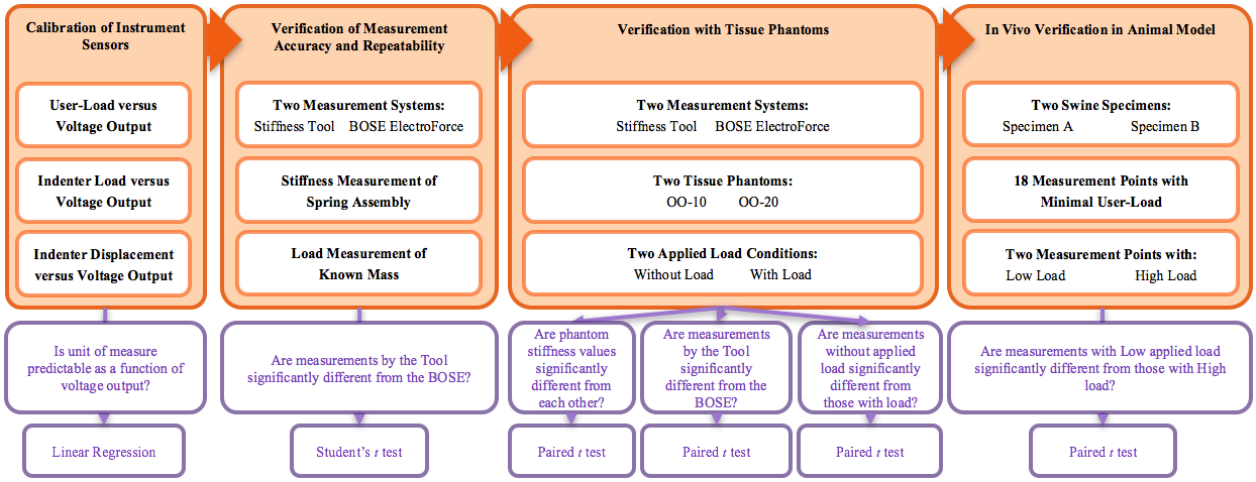

Figure 2.1. Experimental design for the development of a stiffness measurement tool for characterization of abdominal wall tissue

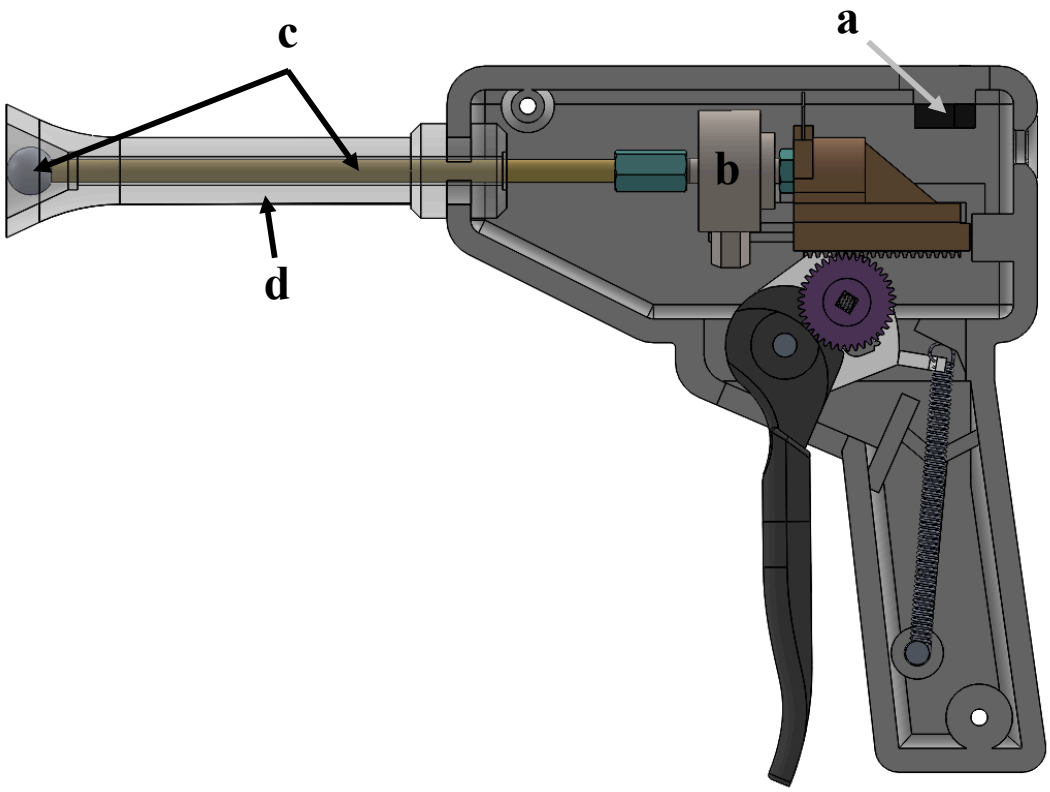

Figure 2.1. Rendering of the stiffness tool prior to design alterations showing internal components and sensors including the indenter displacement (a) and load sensors (b), indenter rod and tip (c), and sheath with reference ring (d)

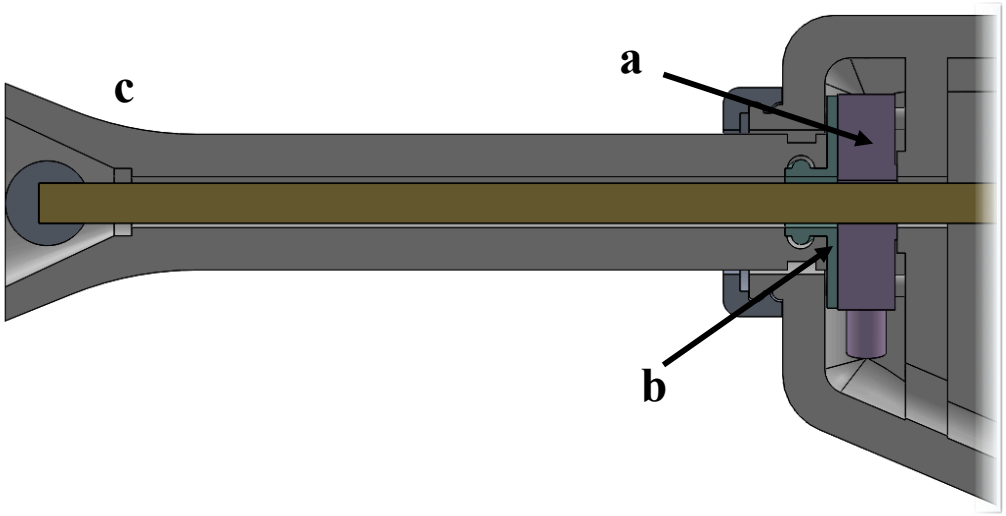

Figure 2.2. Rendered cross-section of the tool after design alteration highlighting the user-load sensor (a), threaded washer (b), and removable sheath with reference ring (c)

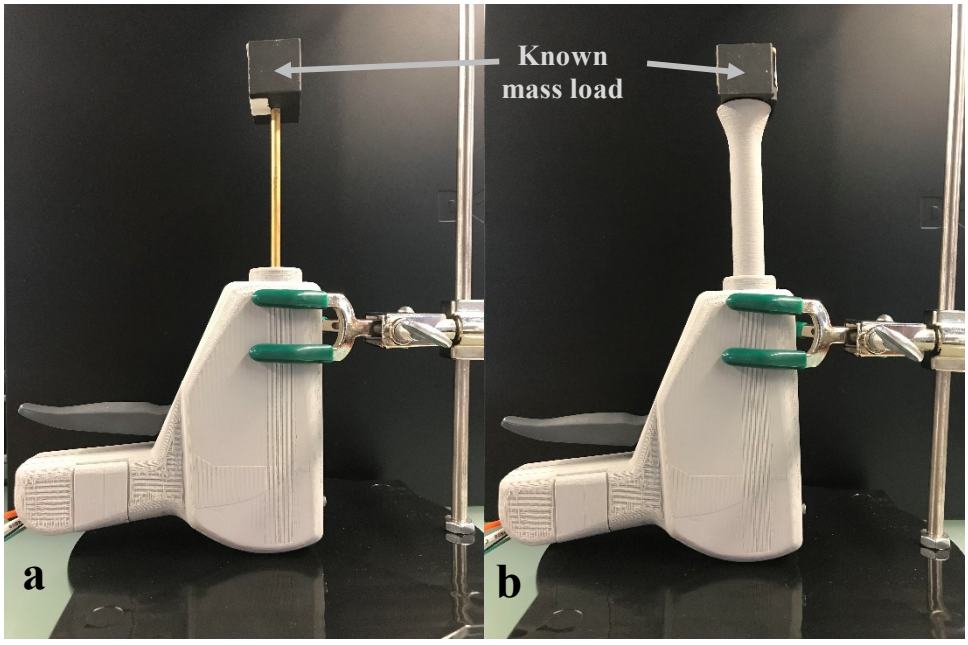

Figure 2.3. Calibration of the stiffness tool's indenter force (a) and user-load (b) sensors


Figure 2.4. Calibration of the stiffness measurement tool's displacement sensor

Figure 2.5. Verification of the tool's accuracy and repeatability using a spring assembly with known stiffness

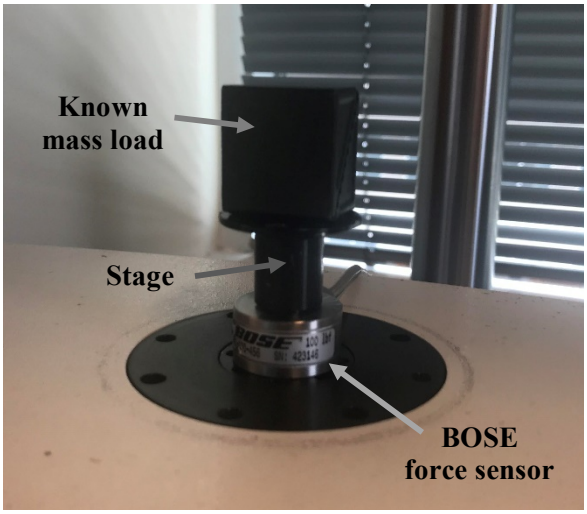

Figure 2.6. A known mass load measured by the BOSE ElectroForce for verification of force data

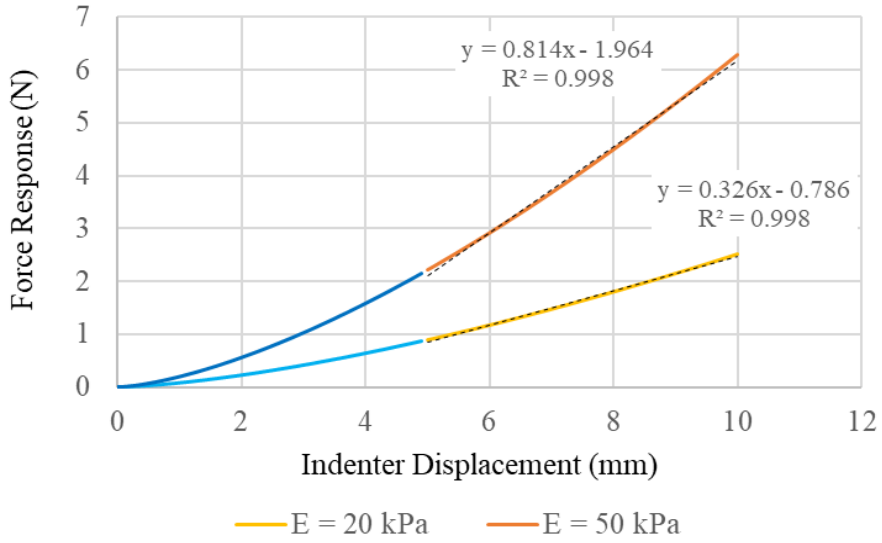

Figure 2.7 Exemplar force-displacement curves of an incompressible tissue under spherical indentation where stiffness is extracted as the slope of the linear region.

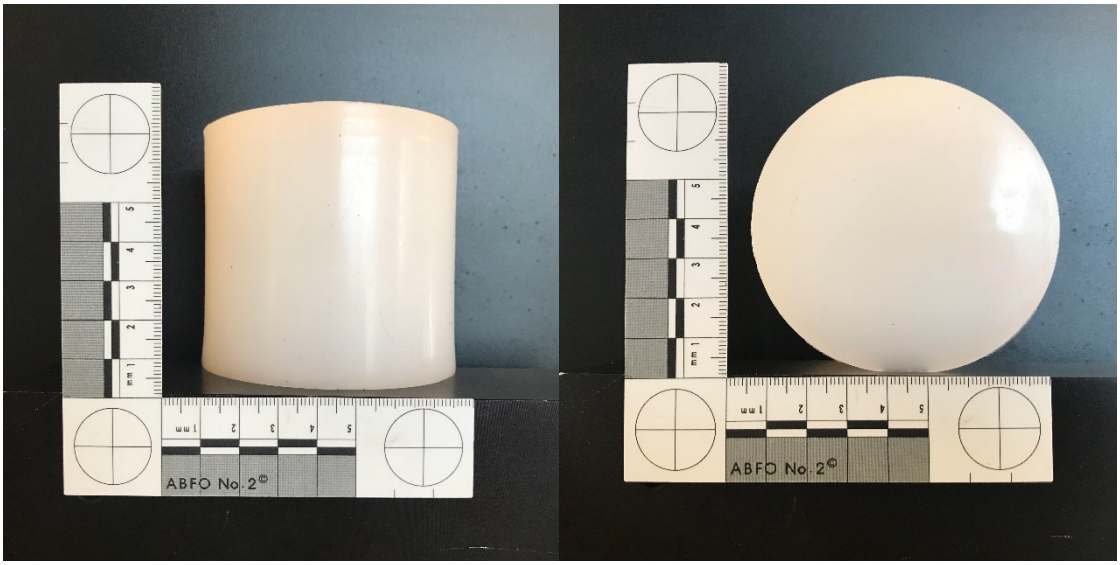

Figure 2.8 Abdominal wall tissue phantom cast from silicone rubber

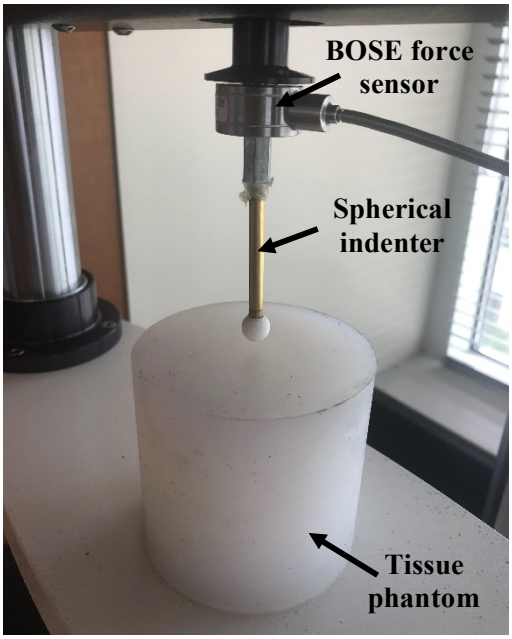

Figure 2.9. Test setup for characterization of tissue phantoms with the BOSE ElectroForce and attached spherical indenter

Figure 2.10 Test setup with stiffness measurement tool attached to Instron load frame for probing tissue phantoms

Figure 2.11. Measurement points arranged across the abdomen of a swine cadaver specimen

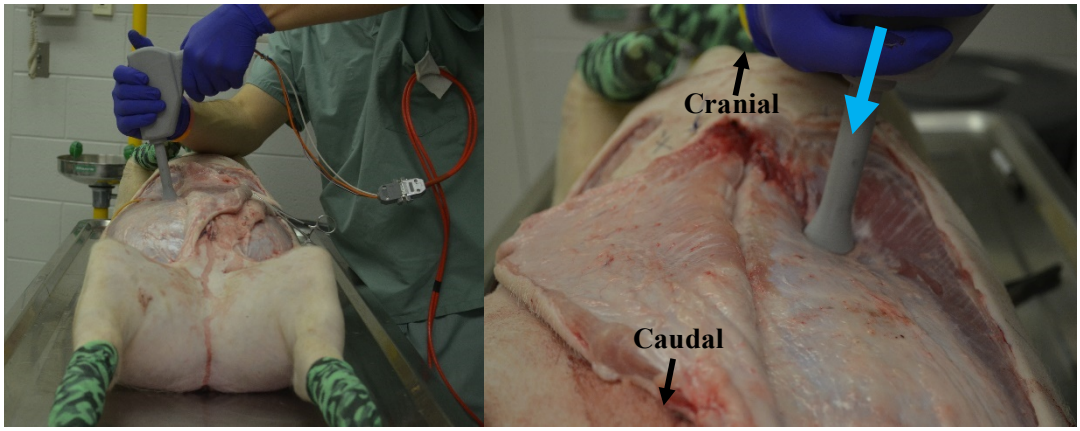

Figure 2.12. Application of the stiffness tool to characterize the abdominal wall of swine cadaver specimens

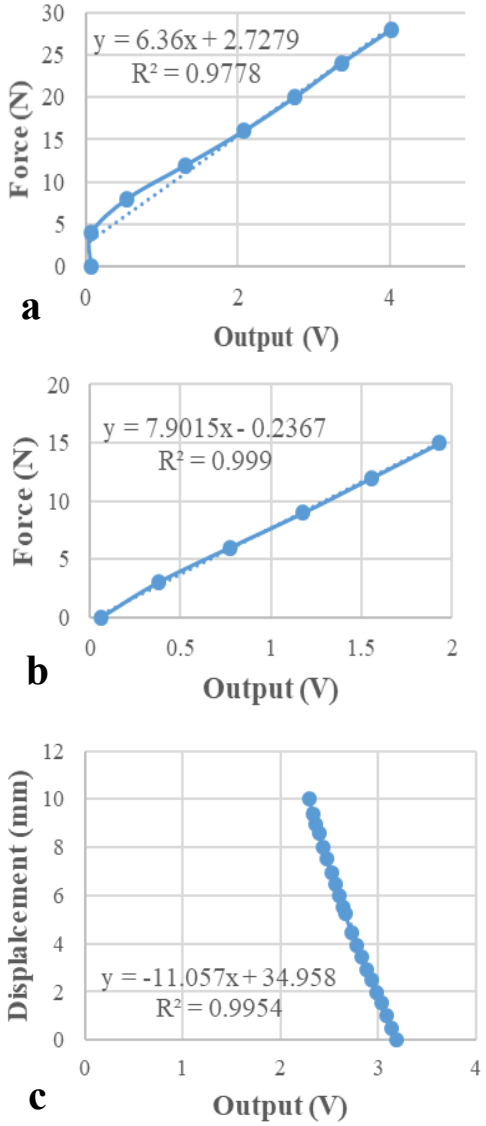

Figure 2.13. Force and displacement versus output voltage calibration curves showing linear relationships for the user-load sensor (a), indenter load sensor (b), and displacement sensor (c)

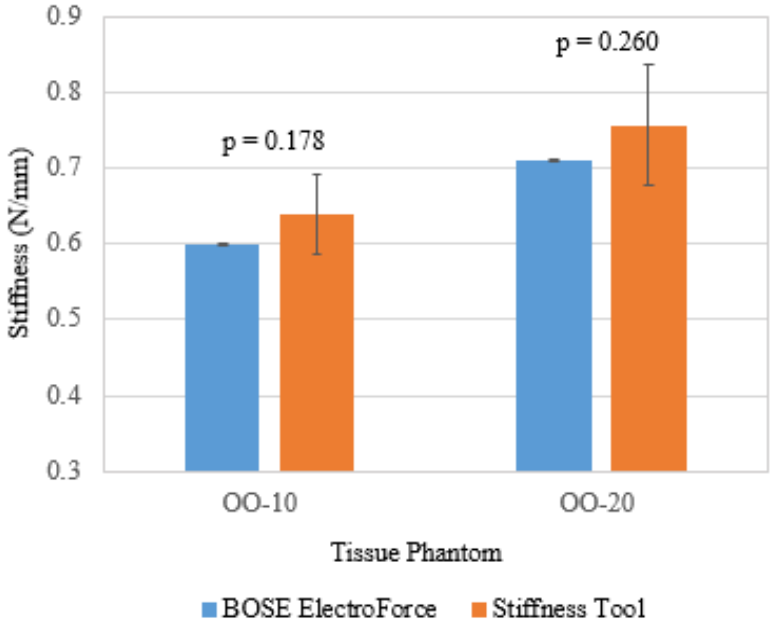

Figure 2.14. Stiffness of two tissue phantom formulations, with no significant differences ($p>0.05$) between measurements from the BOSE and stiffness tool

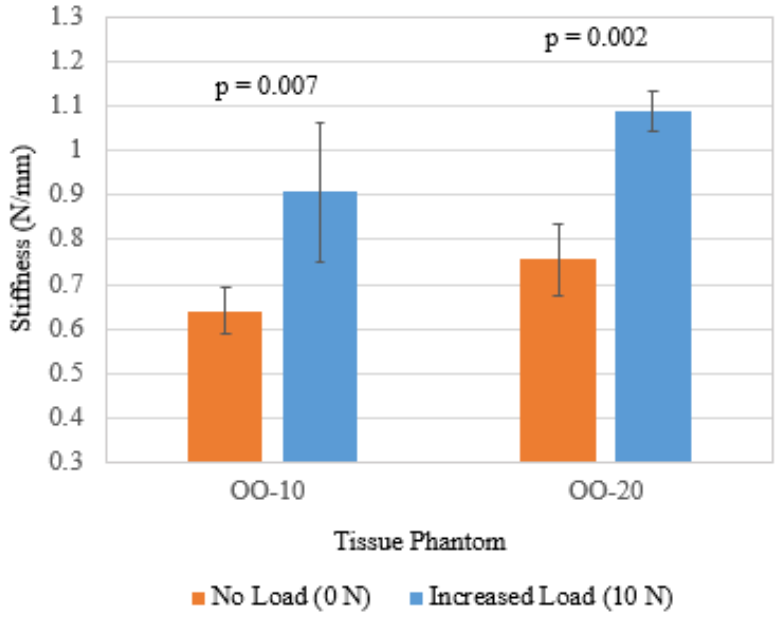

Figure 2.15. Stiffness of two tissue phantom formulations measured by the stiffness tool with significant differences ($p<0.05$) between values acquired under two user-load conditions

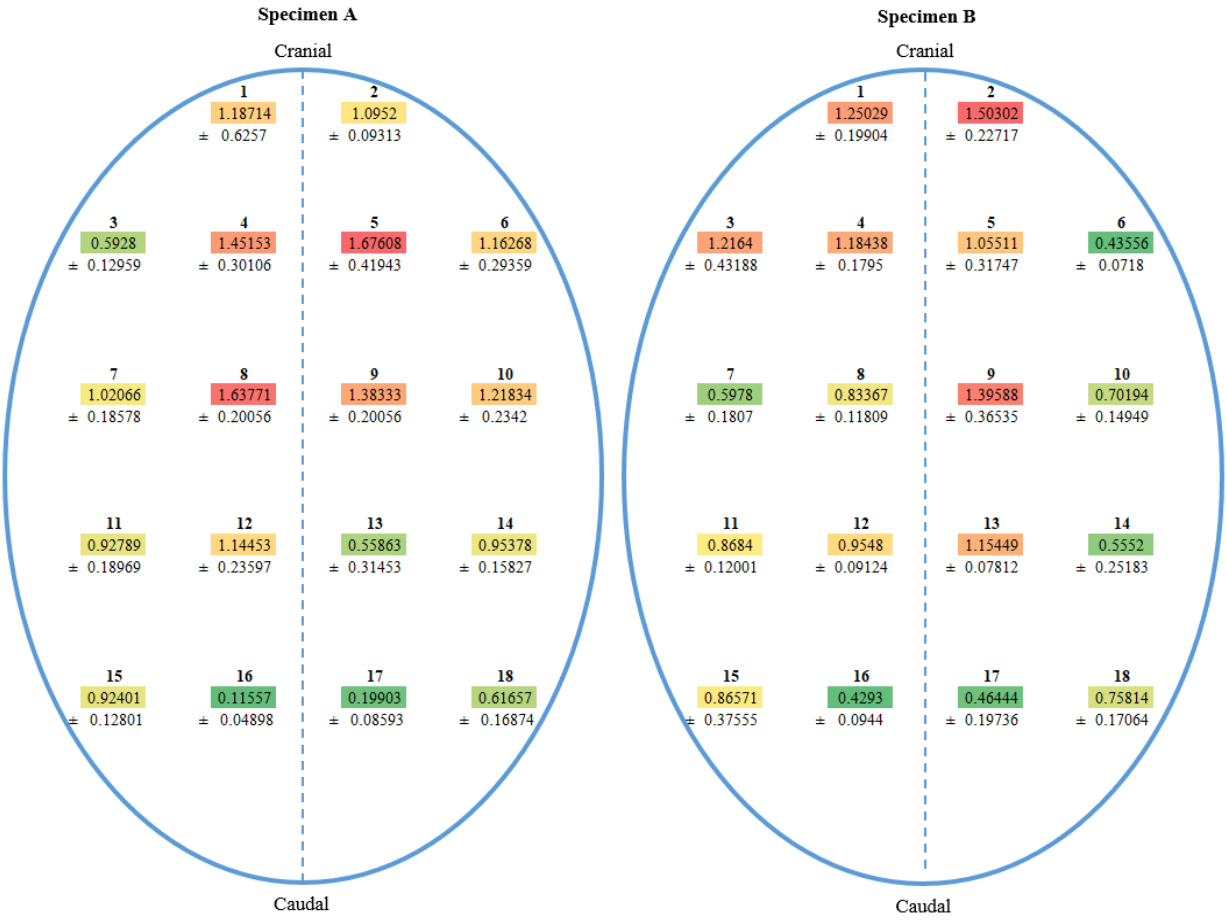

Figure 2.16. Map of abdominal wall stiffness as measured by the tool at 18 points on swine specimens A and B; color coding represents mean stiffness from least (green) to greatest (red)

Table 2.1. Stiffness and applied load measured by the stiffness tool on swine specimens at points 8 and 18 under Low and High load (mean ± standard deviation)

	Specimen A		**Specimen B**	
Point Identifier	8	18	8	18
Stiffness With Low Load (N/mm)	1.63±0.20	0.616±0.168	0.833±0.118	0.758±0.170
Stiffness With High Load (N/mm)	1.64±0.174	2.23±0.549	1.80±0.592	2.61±0.734
Applied Load (N)	8.41±2.60	14.2±5.92	10.2±4.28	13.4±8.68
% Stiffness Increase With Applied Load	0.61%	262%	116%	244%

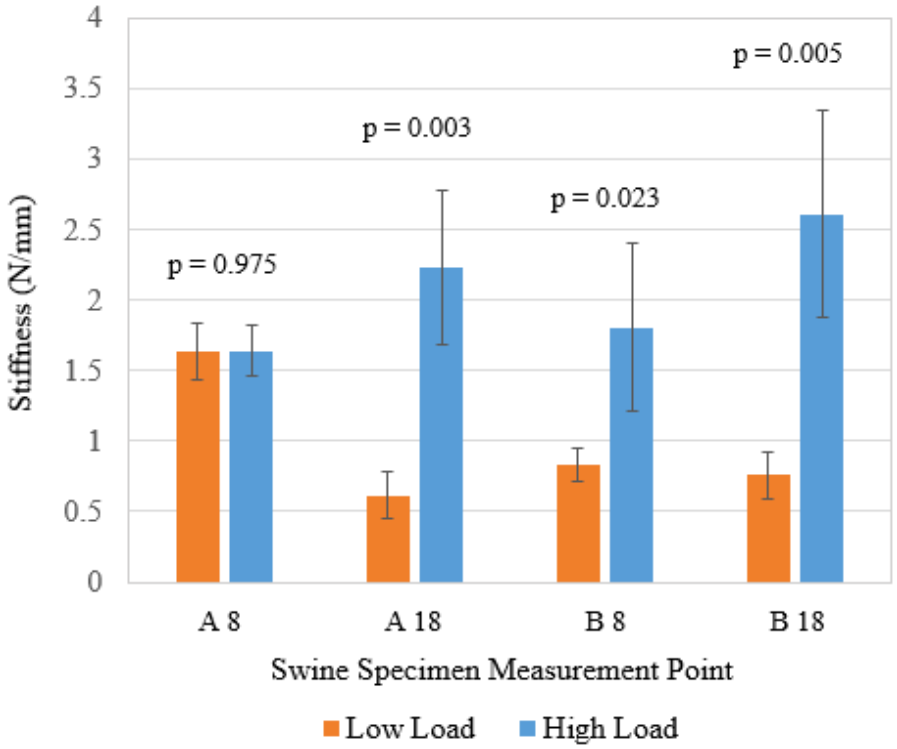

Figure 2.17. Mean stiffness measured by the stiffness tool at points 8 and 18 on swine specimens with significant differences ($p<0.05$) between values acquired under two user-load conditions

CHAPTER THREE

CHARACTERIZATION OF THE MESH-TISSUE COMPOSITE WITH SURGICAL MESH AND TISSUE PHANTOMS

3.1 INTRODUCTION

Successful verification of the stiffness tool and development of tissue phantoms for simulating abdominal wall stiffness provided the necessary tools for characterizing mesh-tissue composites and developing a more accurate model to simulate *in situ* conditions of the abdominal wall reinforced with hernia mesh. This chapter describes the characterization of tissue phantoms in terms of stiffness with and without overlaid mesh as measured by the BOSE and with varied load conditions applied to the stiffness tool. The purpose of this chapter is to address Aim 2 by characterizing mesh-tissue composite stiffness in a uniaxial tension simulator with abdominal wall tissue phantoms and surgical mesh. The experimental design for this chapter is outlined in Figure 3.1.

3.2 METHODS

Characterization of Mesh-Tissue Phantom Composites

A more robust simulation of abdominal wall tissue during hernia repair surgery required a tissue phantom with stiffness within the physiological range, as well as a surgically relevant reinforcement material to mimic mesh implantation. The abdominal wall tissue phantom model established in Chapter Two was expanded to include a surgical mesh sample suitable for hernia repair to overlay tissue phantoms during

indentation. This was achieved by incorporating a custom rig previously developed for applying uniform uniaxial tension to mesh samples overlaying the tissue phantoms.

The system consists of two steel mesh fixation clamps; one rigid and the other allowed to displace along linear bearings. Anisotropic, knit polypropylene mesh sheets (Prolene Soft, Ethicon, New Jersey, USA) were chosen to represent surgically relevant materials. Mesh samples were cut to 100 mm by 175 mm and fixed in the clamps with sandpaper to provide additional friction. Each tissue phantom was placed in the rig with its surface in contact with and parallel to the overlaid mesh sheet (Figure 3.2). The working length of each sheet was measured as the distance between the clamps, parallel to the long axis of the mesh. With phantom and mesh in place, the adjustable clamp was displaced and fixed to apply a static uniaxial tension to the mesh as measured by a hand-held sensor (Portable Electronic Scale, Guangzhou Weiheng Electronics, China). To simulate the *in situ* mesh-tissue composite, four conditions were tested:

1. No mesh; phantoms were tested without mesh as described in Chapter Two.
2. Loose mesh; the mesh sheet was fixed to allow 10% slack in its working length.
3. Zero-tension; applied tension magnitude was only sufficient to flatten the mesh against the phantom's surface.
4. Tight; the mesh sheet was fixed at a tension of 8.2 N/cm of its width, applying less than the approximate 10 N/cm considered too great for textile implants (Klinge 2015).

Non-destructive spherical indentation tests described in Chapter Two were repeated with the BOSE and hand-held stiffness tool on both tissue phantoms under each of the four

mesh tension conditions (Figure 3.3). Stiffness values were extracted from the linear region of each force-displacement curve.

Statistical analysis for comparing stiffness measurements by the BOSE and stiffness tool without an applied load was completed in two phases:

1. Perform paired *t* tests to compare mean stiffness values measured with the BOSE to those measured with the stiffness tool under no applied user-load and obtained on the same tissue phantom and mesh tension condition.
2. Perform one-way repeated-measures ANOVA tests to determine if mesh tension condition (independent variable) was a significant factor affecting the mean stiffness values (dependent variable) acquired from testing with the BOSE and stiffness tool.

Verification with Mesh-Tissue Phantom Composites

In addition to testing without a user-load for comparison to the BOSE, the stiffness tool was used to characterize the mesh-phantom composites under varied applied user-load. To evaluate the effects of user-load on stiffness measurements, a range of forces were applied to the tool within the Instron test frame prior to indentation on each phantom and mesh tension condition (Figure 3.4). This was achieved by displacing the tool into the composite sample, effectively applying a known load and holding the tool rigid throughout indentation. Four applied user-load conditions included Zero-load (0 N), Low load (6 N), Medium load (10 N), and High load (14 N). With each applied load, the tool was used to probe the mesh-phantom composites five times to a depth of 10

mm at a rate of 10 mm/s. Stiffness values were again calculated as the slope of the linear region of the force-displacement curves. To again confirm accuracy of user-load measurements, paired *t* tests were used to determine if the applied load magnitudes measured by the stiffness tool differ significantly from the actual load magnitudes applied by the Instron prior to indentation across all four mesh tension conditions on both tissue phantoms.

Measured stiffness values were effectively normalized by identifying a constant reduction factor corresponding to each load condition and reducing the indenter force values of each force-displacement curve acquired under an applied load by that constant. Reduction factors were first calculated as the percent increase in measured stiffness from No Load to each of the three subsequent user-load conditions. Normalized stiffness values were extrapolated from the linear region of these new force-displacement curves and the difference between normalized stiffness values and those measured without user-load were averaged for each load condition across all mesh-phantom composites. Reduction factors were then optimized for each load condition by adjusting their magnitude to minimize the average difference between stiffness values measured without user-load and corresponding normalized values. Linear regression was performed to define a model for optimized factors expressed as a percentage (y) as a function of corresponding measured user-loads (x) and an R^2 value was used to evaluate linearity.

Evaluation of user-load effects and comparison of normalized stiffness values to those acquired without an applied load was accomplished through statistical analysis completed in three phases:

1. Perform one-way repeated-measures ANOVA tests to determine if user-load condition (independent variable) was a significant factor affecting the mean stiffness values (dependent variable) acquired for each mesh tension on the same tissue phantom.
2. Perform linear regression to evaluate the relationship between measured stiffness and load applied to the stiffness tool across all four mesh tension conditions on both tissue phantoms.
3. Perform one-way ANOVA tests to determine if user-load condition (independent variable) was a significant factor affecting mean normalized stiffness values (dependent variable) acquired for each mesh tension on the same tissue phantom.

3.3 RESULTS

Characterization of Mesh-Tissue Phantom Composites

Mesh-tissue phantom composites were successfully characterized in terms of stiffness from indentation tests with the BOSE ElectroForce system and hand-held stiffness tool. Stiffness values were extrapolated from the linear region of each force-displacement curve through linear regression in the range from 5 to 10 mm of indentation. A linear fit was observed with $R^2>0.9$ for all measurements.

Half of the mean stiffness measurements by both measurement systems on the same tissue phantom and across mesh tension conditions were not significantly different from one another (paired *t* test, $p>0.05$) (Figure 3.5 and 3.6). Stiffness values measured with a "Tight" mesh condition on both tissue phantoms showed greater difference

between the BOSE and hand-held stiffness tool as well as higher degree of error seen in standard deviations for both measurement instruments (Tables 3.1 – 3.3). Overall, with a condition of greater tension and subsequently greater stiffness, measurements by the tool were lower and significantly different (paired *t* test, $p=0.001$) from those by the BOSE.

Analysis revealed that at least one mesh tension condition had a significantly different ($p<0.05$) mean stiffness for both tissue phantoms (Table 3.4). Stiffness values across all mesh tension conditions measured by the same instrument were significantly different (Tukey, $p<0.05$) except between "Loose mesh" and" Zero-Tension mesh" on the OO-10 tissue phantom as measured by the stiffness tool (Table 3.5 and 3.6). All mean stiffness values were shown to increase with uniaxial tension applied to the overlaying mesh sample. Therefore, both measurement instruments were able to characterize the mesh-tissue phantom composites and show a change in measured stiffness with an increase in tension of the mesh.

Verification with Mesh-Tissue Phantom Composites

Further verification of the stiffness tool and evaluation of the effects of user-load on measured stiffness was accomplished through a more robust experimental design and subsequent statistical analysis. Mesh-tissue phantom composites were successfully characterized in terms of stiffness with a range of loads applied to the hand-held tool prior to indentation.

Most mean load measurements were significantly different (*t* test, $p<0.05$) from the actual load magnitude applied by the Instron (Table 3.7and 3.8). However, little

variation was observed in load measurements as evidenced by standard deviations of at most 0.1 N (Table 3.9 and 3.10). Despite small standard deviations in load measurement, actual load magnitudes were used in lieu of measured values for subsequent analysis and evaluation of the relationship between applied load and measured stiffness.

The stiffness tool was able to distinguish a difference between stiffness measurements under different loads applied during operation. Load conditions were a significant factor effecting mean stiffness for each tissue-phantom composite combination (Table 3.11). For Zero-load and Low Load conditions, mean stiffness values measured by the tool were significantly different (Tukey's test, $p<0.05$) from those acquired on the same mesh tension overlay under different applied load conditions. Stiffness values measured under Medium (10 N) and High Load (14 N) were not significantly different (Table 3.12 and 3.13).

An increase in measured stiffness was highly predictable with an increase in user-load applied to the tool. The relationship between stiffness and increased applied load was highly linear ($R^2>0.9$) except for one mesh-phantom combination ($R^2=0.84$) (Figures 3.7 and 3.8). Additionally, percent change in measured stiffness versus applied load also was highly linear ($R^2>0.9$) for all mesh-phantom composites (Figure 3.9). Therefore, change in measured stiffness was also highly predictable with an increase in applied load.

A simple linear model was adequate for correcting measured stiffness values with a known applied load. Optimized reduction factors for normalizing measured stiffness under No load, Low, Medium, and High load were 0%, 25.8%, 34.5%, and 40.1%, respectively. These were used as factors by which each stiffness value acquired under the

corresponding user-load would be reduced to a value near stiffness measured by tool without user-load. Using these optimized reduction factors, the change in stiffness versus user-load was highly linear related (R^2=0.9407), similar to that of the No mesh and Tight mesh conditions (Figure 3.10).

User-load conditions were not a significant factor effecting most mean normalized stiffness values. Analysis revealed that there were no significant differences (ANOVA, $p>0.05$) among normalized mean stiffness values from three mesh tension conditions between the two tissue phantoms (Table 3.14). For those mesh-phantom composite conditions in which user-load was a factor effecting normalized values, only one-third of the remaining normalized stiffness values were significantly different (Tukey's test, $p<0.05$) from those acquired without applied load (Tables 3.15 and 3.16). Therefore, 75% of stiffness values were successfully normalized with no difference from measured stiffness without applied user-loads.

3.4 CONCLUSIONS

Abdominal wall mesh-tissue phantom composites were successfully characterized in terms of stiffness as measured by the BOSE benchtop system and hand-held stiffness tool thereby satisfying Aim 2 of this thesis. Both the BOSE system and stiffness tool were able to clearly distinguish an increase in stiffness with the presence of mesh. Simulation of surgical mesh attached to the abdominal wall was achieved by fixing mesh samples within a uniaxial rig to overlay tissue phantoms. Probing the mesh-phantom composites with a range of loads applied to the tool during indentation revealed a linear

and predictable relationship between an increase in measured stiffness and increase in applied user-load. These relationships also showed that as mesh tension increased, user-load had a greater impact on measured stiffness until a point at which mesh tension was so great that user-load had a less significant impact and changes in stiffness resembled those on a tissue phantom without mesh.

Through evaluation of user-load effects, a linear model was established to correct an increase in measured stiffness as a function of applied user-load, effectively normalizing measurements to within an average 12% error of stiffness measured without user-load. For further characterization of the mesh-tissue composite with the stiffness tool, it may be desirable to set acceptable criteria for accurate measurements such as 6 to 10 N of applied load prior to indentation. The method used in this thesis of applying user-loads prior to indentation and holding the tool rigid was assumed to be the most intuitive for a user and most reasonable to simulate experimentally. The effects of applied load on stiffness measurement may vary with user interactions in which the tool is held rigid during indentation, is displaced to maintain a constant load on the reference ring, displaced at the same rate as the indenter, or any combination thereof which may cause displacement of the indenter into tissue to be greater than 10 mm.

Although tempting to propose the addition of a motorized actuation mechanism, measurements obtained with the hand-held stiffness tool were highly accurate and repeatable when compared to standard benchtop equipment and user-induced effects on stiffness measurements were successfully reduced. What's more, additional instrumentation would increase the overall cost, weight, and power consumption of the

stiffness tool. However, small indicators such as an on-board LED light may be useful to inform the user of too much or too little load applied to the tool. Similarly, the user-load sensor may be replaced by a more simple spring mechanism in which the user is required to compress a spring to a predetermined position prior to indenting, thereby applying a known load calculated using a spring constant.

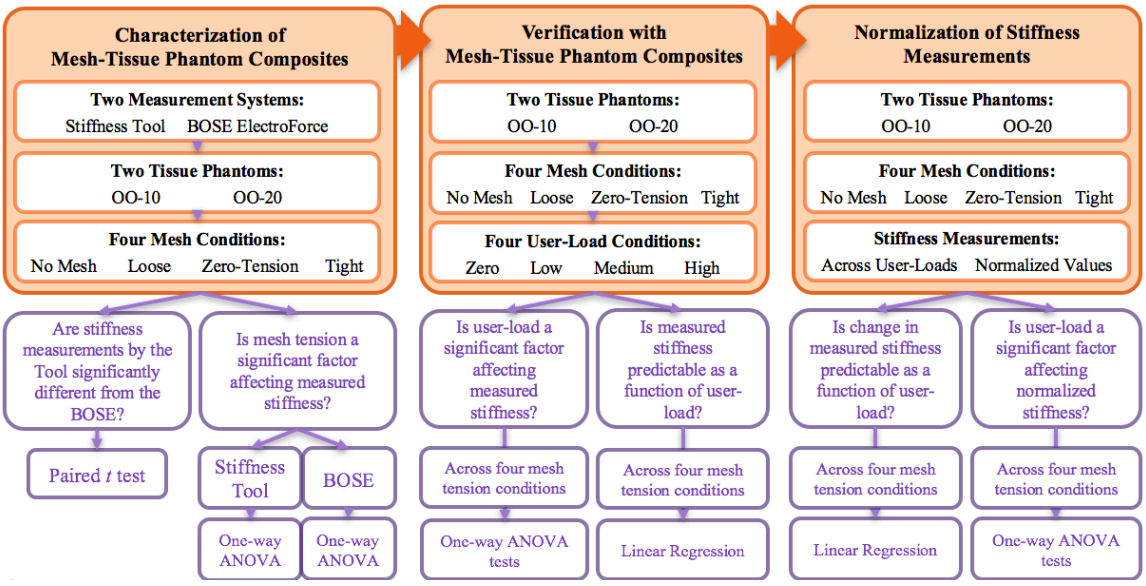

Figure 3.1. Experimental design for characterization of the mesh-tissue composite with surgical mesh and tissue phantoms

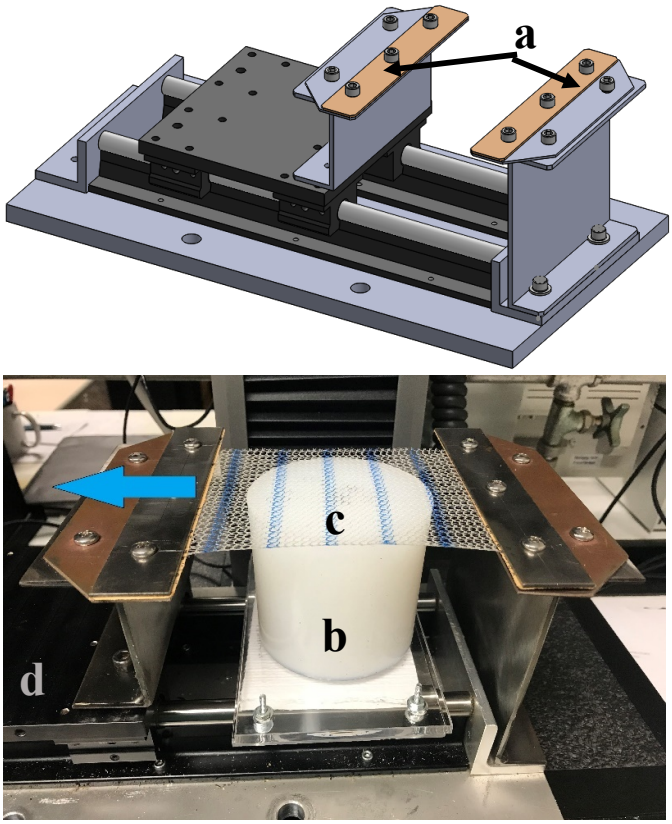

Figure 3.2. Uniaxial tension rig consisting of fixation clamps (a), tissue phantom (b), mesh sample (c), and moveable carriage (d) with applied tension

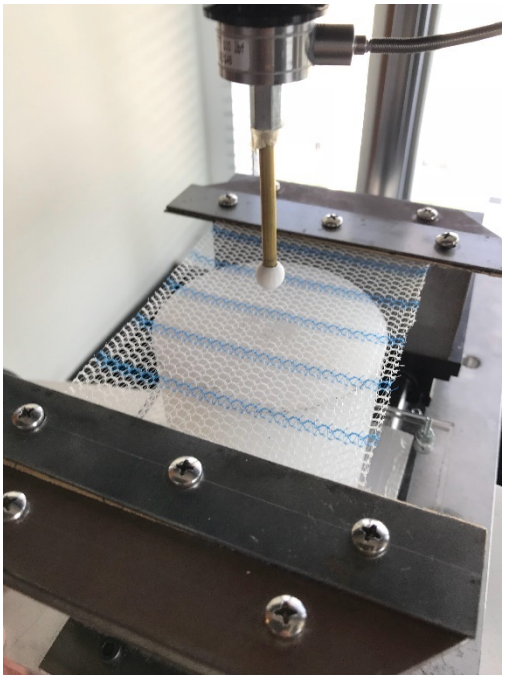

Figure 3.3. Test setup for indentation of the mesh-phantom composite under the BOSE ElectroForce and attached spherical indenter

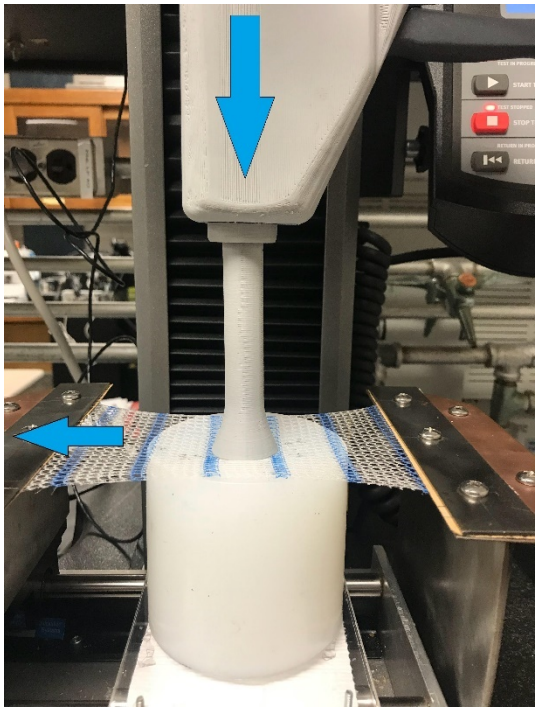

Figure 3.4. Test setup for indentation of the mesh-phantom composite with the stiffness tool under applied load

Table 3.1. Stiffness values of tissue phantoms with and without mesh overlay measured by the BOSE (mean ± standard deviation)

Phantom Identifier	No Mesh	Loose	Zero-Tension	Tight
OO-10	0.599±0.001	0.783±0.007	1.16±0.010	2.10±0.033
OO-20	0.709±0.001	0.992±0.002	1.30±0.003	2.87±0.052

Table 3.2. Stiffness values of the OO-10 phantom with varied mesh tension conditions measured by the tool under varied user-load (mean ± standard deviation)

Mesh Condition / User-Load Condition	No Mesh	Loose	Zero-Tension	Tight
Zero	0.639±0.052	0.791±0.091	0.982±0.131	1.70±0.089
Low	0.777±0.075	1.16±0.164	1.64±0.147	2.30±0.065
Medium	0.906±0.156	1.49±0.096	2.02±0.103	2.61±0.111
High	0.961±0.041	1.62±0.142	2.26±0.186	2.89±0.115

Table 3.3. Stiffness values of the OO-20 phantom with varied mesh tension conditions measured by the tool under varied user-load (mean ± standard deviation)

Mesh Condition / User-Load Condition	No Mesh	Loose	Zero-Tension	Tight
Zero	0.756±0.080	1.08±0.048	1.30±0.008	1.99±0.138
Low	1.03±0.047	1.32±0.111	1.85±0.072	2.29±0.105
Medium	1.08±0.046	1.54±0.127	2.17±0.045	2.55±0.088
High	1.10±0.022	1.67±0.072	2.18±0.180	2.61±0.292

Table 3.4. ANOVA comparing stiffness values for each mesh tension condition on both tissue phantoms

Measurement Instrument	BOSE ElectroForce	Stiffness Tool
Phantom OO-10	<0.001	<0.001
Phantom OO-20	<0.001	<0.001

Table 3.5. Tukey's post hoc tests comparing stiffness values measured by the BOSE for each mesh tension condition on both tissue phantoms

Mesh Condition Comparison	No mesh/ Loose	No mesh/ Zero-Tension	No mesh/ Tight	Loose/ Zero-Tension	Loose/ Tight	Zero-Tension/ Tight
Phantom OO-10	<0.001	<0.001	<0.001	<0.001	<0.001	<0.001
Phantom OO-20	<0.001	<0.001	<0.001	<0.001	<0.001	<0.001

Table 3.6. Tukey's post hoc tests comparing stiffness values measured by the stiffness tool for each mesh tension condition on both tissue phantoms

Mesh Condition Comparison	No mesh/ Loose	No mesh/ Zero-Tension	No mesh/ Tight	Loose/ Zero-Tension	Loose/ Tight	Zero-Tension/ Tight
Phantom OO-10	0.006	0.006	<0.001	0.080	<0.001	<0.001
Phantom OO-20	0.003	<0.001	<0.001	<0.001	<0.001	<0.001

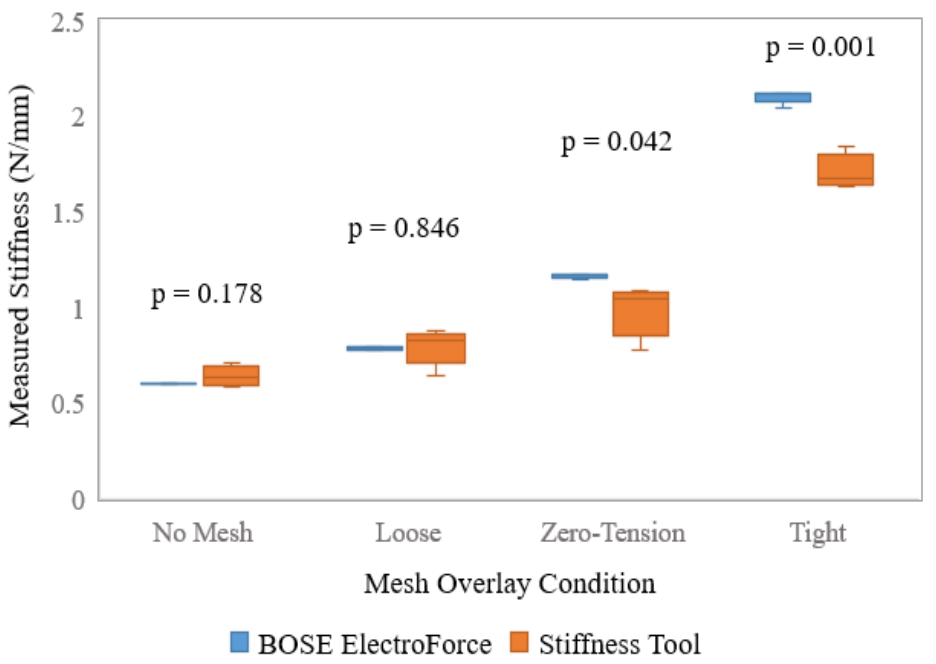

Figure 3.5. Stiffness of the OO-10 tissue phantom with significant differences ($p<0.05$) between measurements by the BOSE and hand-held stiffness tool across mesh tension conditions

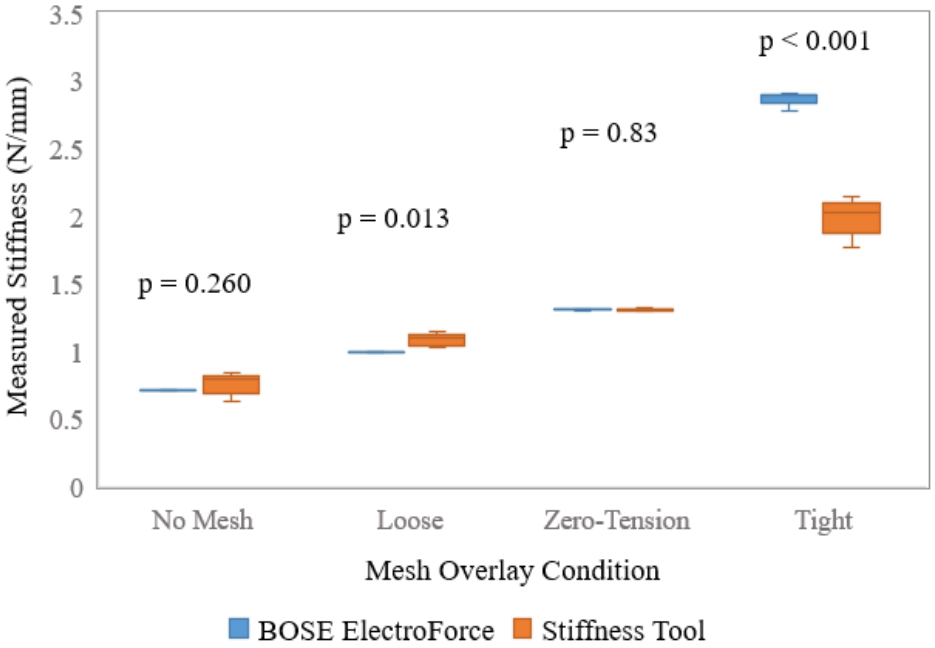

Figure 3.6. Stiffness of the OO-20 tissue phantom with significant differences ($p<0.05$) between measurements by the BOSE and hand-held stiffness tool across mesh tension conditions

Table 3.7. Paired *t* tests comparing measured and actual user-loads applied to the stiffness tool on the OO-10 phantom

	No Mesh	Loose	Zero-Tension	Tight
Low (6 N)	<0.001	0.001	0.005	0.010
Medium (10 N)	<0.001	0.003	<0.001	0.445
High (14 N)	0.001	0.027	0.072	0.072

Table 3.8. Paired *t* tests comparing measured and actual user-loads applied to the stiffness tool on the OO-20 phantom

	No Mesh	Loose	Zero-Tension	Tight
Low (6 N)	0.003	0.002	0.001	0.199
Medium (10 N)	0.286	0.010	0.010	<0.001
High (14 N)	0.005	0.797	0.029	0.009

Table 3.9. Applied user-loads measured by the stiffness tool prior to indentation on the OO-10 phantom (mean ± standard deviation)

Mesh Condition / **User-Load Condition**	**No Mesh**	**Loose**	**Zero-Tension**	**Tight**
Low (6 N)	3.98±0.070	4.76±0.346	4.75±0.496	5.06±0.451
Medium (10 N)	8.77±0.265	8.15±0.622	9.01±0.167	9.84±0.415
High (14 N)	12.3±0.456	13.2±0.463	13.5±0.420	14.7±0.560

Table 3.10. Applied user-loads measured by the stiffness tool prior to indentation on the OO-20 phantom (mean ± standard deviation)

Mesh Condition / **User-Load Condition**	**No Mesh**	**Loose**	**Zero-Tension**	**Tight**
Low (6 N)	4.44±0.560	4.52±0.443	4.21±0.504	5.56±0.629
Medium (10 N)	9.63±0.670	8.75±0.597	8.61±0.669	11.0±0.171
High (14 N)	13.0±0.383	14.0±0.423	12.3±1.08	14.6±0.286

Table 3.11. ANOVA comparing measured stiffness across four load conditions on each mesh-phantom composite

Tissue Phantom Identifier	OO-10	OO-20
No Mesh	<0.001	<0.001
Loose	<0.001	<0.001
Zero-Tension	<0.001	<0.001
Tight	<0.001	<0.001

Table 3.12. Tukey's post hoc tests comparing stiffness values measured on OO-10 phantom-mesh combinations across four applied load conditions

Load Condition Comparison	Zero/ Low	Zero/ Medium	Zero/ High	Low/ Medium	Low/ High	Medium/ High
No Mesh	0.038	0.011	<0.001	0.157	0.002	0.086
Loose	0.018	<0.001	0.001	0.036	0.013	0.174
Zero-Tension	0.001	<0.001	<0.001	0.014	0.007	0.097
Tight	0.001	<0.001	<0.001	0.008	<0.001	0.003

Table 3.13. Tukey's post hoc tests comparing stiffness values measured on OO-20 phantom-mesh combinations across four applied load conditions

Load Condition Comparison	Zero/ Low	Zero/ Medium	Zero/ High	Low/ Medium	Low/ High	Medium/ High
No Mesh	0.003	<0.001	0.001	0.211	0.049	0.557
Loose	0.007	0.001	<0.001	0.027	0.006	0.181
Zero-Tension	<0.001	<0.001	<0.001	0.002	0.005	0.956
Tight	0.021	<0.001	0.017	0.004	0.054	0.658

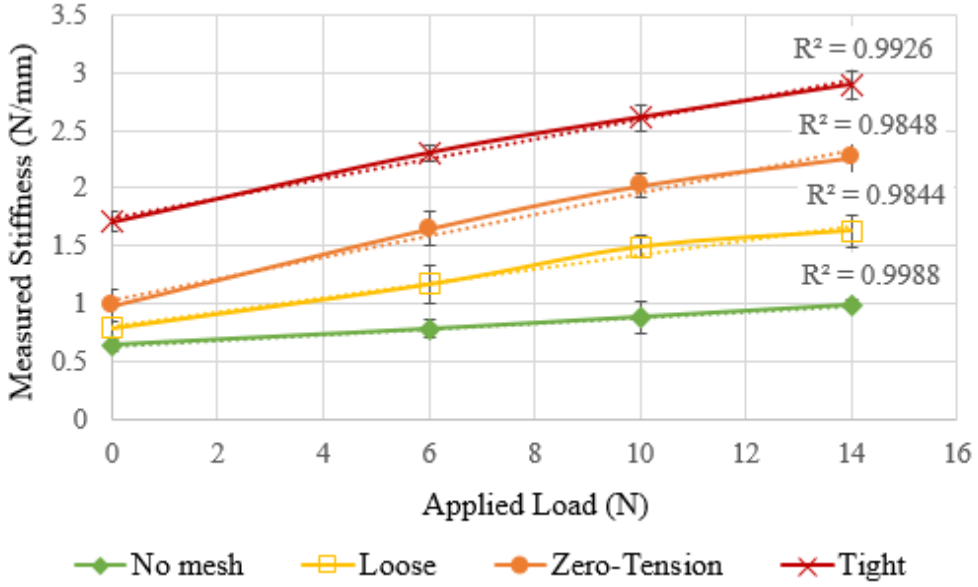

Figure 3.7. Measured stiffness versus applied load on the OO-10 phantom across four mesh conditions

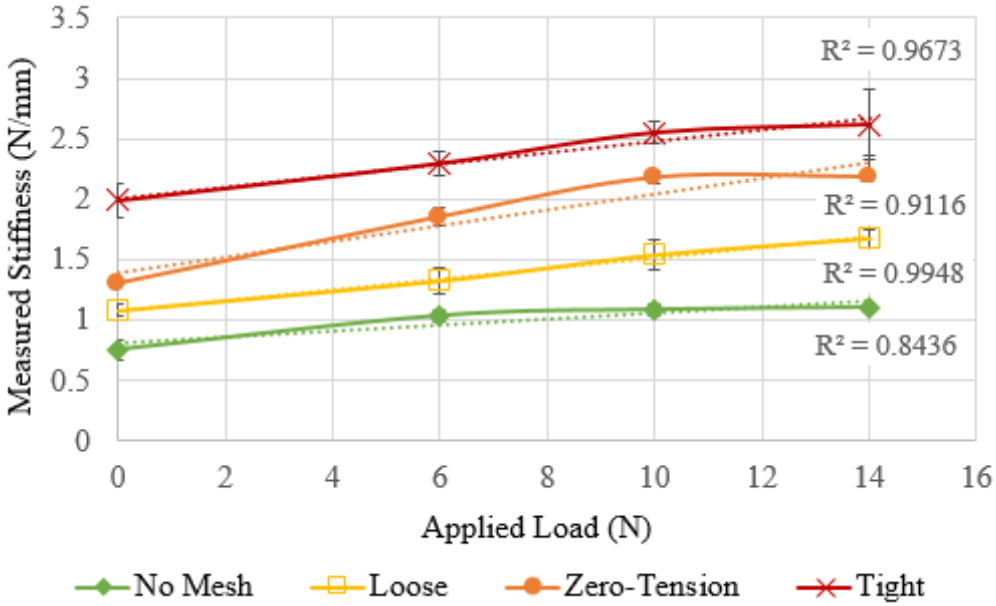

Figure 3.8. Measured stiffness versus applied load on the OO-20 phantom across four mesh conditions

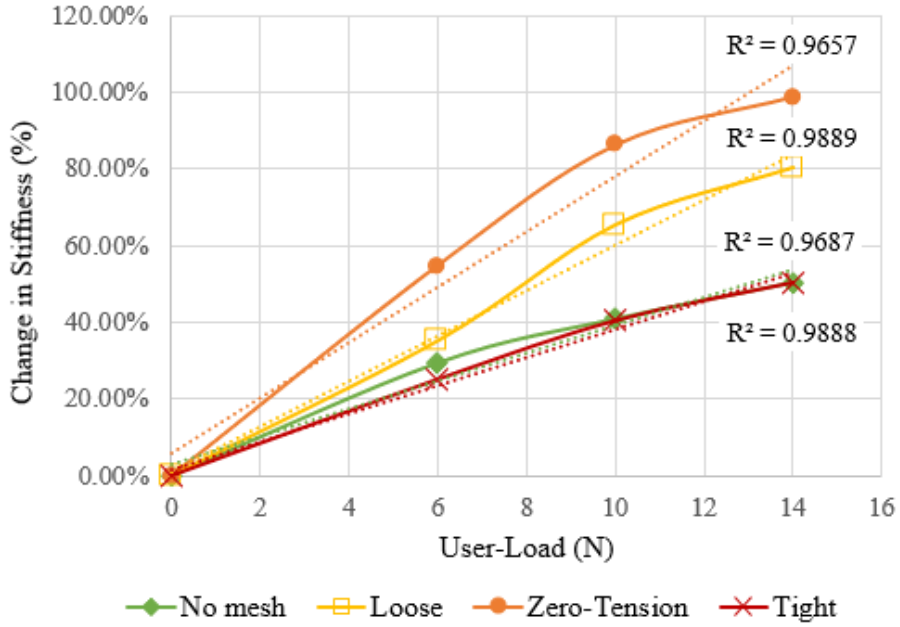

Figure 3.9. Percent change in measured stiffness versus applied load showing high linearity across four mesh conditions on both tissue phantoms

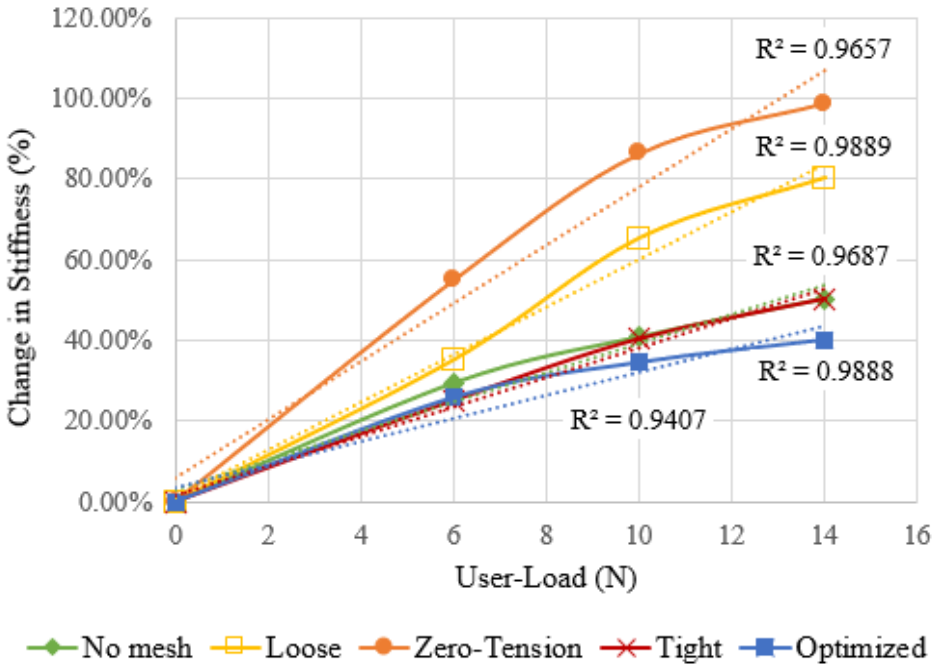

Figure 3.10. Change in measured stiffness versus applied load overlaid with optimized correction factors for normalizing stiffness measurements

Table 3.14. ANOVA comparing normalized stiffness values for each mesh tension condition on both tissue phantoms

Tissue Phantom Identifier	OO-10	OO-20
No Mesh	0.347	0.001
Loose	0.030	0.108
Zero-Tension	0.005	0.001
Tight	0.954	0.009

Table 3.15. Tukey's tests comparing normalized mean stiffness values measured on OO-10 phantom-mesh combinations across four applied load conditions

Load Condition Comparison	Zero/ Low	Zero/ Medium	Zero/ High	Low/ Medium	Low/ High	Medium/ High
No Mesh			See ANOVA			
Loose	0.406	0.020	0.053	0.212	0.214	0.980
Zero-Tension	0.024	0.011	<0.001	0.185	0.173	0.674
Tight			See ANOVA			

Table 3.16. Tukey's tests comparing normalized mean stiffness values measured on OO-20 phantom-mesh combinations across four applied load conditions

Load Condition Comparison	Zero/ Low	Zero/ Medium	Zero/ High	Low/ Medium	Low/ High	Medium/ High
No Mesh	0.768	0.208	0.060	0.027	0.004	0.048
Loose			See ANOVA			
Zero-Tension	0.039	<0.001	1.000	0.170	0.109	0.089
Tight	0.018	0.003	0.019	0.311	0.120	0.284

CHAPTER FOUR

DEVELOPMENT OF A BENCHTOP SYSTEM TO SIMULATE BIAXIAL LOADING OF MESH-PHANTOM COMPOSITES

4.1 INTRODUCTION

The most widely used method of stiffness characterization for materials is based on their force-displacement response under non-destructive indentation as established in previous chapters. In addition to reported stiffness values, the abdominal wall also has a resting internal pressure near 21 mmHg (~0.4 psi) (Song 2006a, Song 2006b, Mitchell 2011). Complexity of abdominal wall behavior is further highlighted by a change in shape from a cylinder to a dome during changes in posture and activity (Hodges 2000). Considering the complex behavior of soft tissues and the various factors in their mechanical behavior, simulation of the abdominal wall requires tissue phantom materials representative of physiological tissues and loading conditions. The uniaxial tension system described in Chapter Two is limited by a static stiffness of the underlying phantom and boundary conditions of the mesh material under uniaxial tension. A more robust biaxial system can allow controlled variation in the stiffness and tension of a mesh-phantom composite in correlation with a wider range of simulated physiological conditions. The purpose of this chapter is to address Aim 3 by developing a benchtop simulator to mimic abdominal wall distension and provide biaxial loading of mesh-phantom composites. The experimental design for this chapter is outlined in Figure 4.1.

4.2 METHODS

Inflation Technique for Biaxial Loading

Simulating the behavior of the abdominal wall and mesh-tissue composite under physiological conditions requires loading beyond standard uniaxial tension. Applying forces perpendicular to the mesh-tissue plane induces a distensional load mimicking physiological biomechanics better than uniaxial testing (Cobb 2009, Konerding 2012). With this approach, perpendicular force applied to a constrained material can be used as a more robust method of characterizing the mesh-tissue composite.

A common mechanical test used in the textile industry is the constant-rate-of-extension ball burst test (ASTM International 2011 D6797 -15) which has been applied for the characterization of soft tissues and mesh (Freytes 2005, Konerding 2012). This test consists of a spherical indenter extended perpendicularly into a membranous material constrained by a clamping ring. The clamp serves as a circular constraint with known diameter to maintain a plane through which the sample is loaded to failure. A similar constraint setup has been applied to study mesh mechanics under non-destructive biaxial load induced by internal pressure beneath a sample membrane (Rohrnbauer 2013, Maurer 2014, Sahoo 2014). With an inflated membrane under known constraints and loading conditions, a range of stiffness values can be achieved and characterized by non-destructive indentation. This rationale serves as the basis for the development of an inflation device capable of simulating abdominal distension and biaxial loading of mesh-phantom composites across a range of physiological pressure and stiffness.

Biaxial Loading of Tissue Phantoms

Thin tissue phantom membranes were created from standard latex resistance bands (Stamina Products, Springfield, MO). These latex bands, commonly used in physical conditioning, are described as having a linear stress-elongation relationship up to 100% elongation and are coded in various colors corresponding to a range of elastic resistance and tensile moduli. The chosen green latex resistance bands have an elastic resistance of 4.3±0.16 N and modulus of 2.47±0.09 MPa (Santos 2009). Tissue phantoms created from the latex were cut into square samples at 100 mm in length and width with a thickness of 0.45 mm.

For the biaxial mechanical characterization of tissue phantom membranes, a custom-built benchtop apparatus was developed to simulate physiological pressure and distension inspired by the work of a German group and others using a similar inflation technique (Rohrnbauer 2013, Haller 2011). The benchtop simulator was custom designed (SolidWorks 2017, Dassault Systemes, France) and manufactured from Delrin (polyoxymethylene), consisting of an upper plate, a second supporting plate, pressure chamber, air inlet, and attached high-accuracy pressure gauge (4026K27, 0-5 psi, 0.1 increments, McMaster-Carr, USA) seen in Figure 4.2. Both plates secured atop the chamber contain a central circular hole used to limit phantom sample diameter with options including 33 mm and 63 mm. Phantom membranes were clamped with rings of sandpaper and centered between the plates, thereby creating a closed pressure chamber.

Characterization of tissue phantom membranes in terms of stiffness was performed similarly to the mechanical testing protocol described in previous chapters of

this thesis. To first create physiologically relevant pressure, a portable pressurized tank (FP209592DI, 100 max psi, Campbell Hausfeld, Ohio, USA) was used to pump air into the chamber, applying a static pressure, and effectively inflating the phantom membrane. Static pressure ranging from 0.4 to 1.6 psi (21 to 83 mmHg) was applied at increments of 0.1 psi (5.1 mmHg). The spherical indenter attached to the ElectroForce was lowered to the apex of the inflated membrane to track apical position. Vertical displacement of each membrane was calculated as the difference between the initial non-inflated position and the height of their apex once inflated. The applied pressure and corresponding vertical displacement were recorded and phantoms were indented 5 times to 10 mm at a rate of 10 mm/s (Figure 4.3). Indentation testing was performed on single and double layer membranes constrained under each of the two upper-plate hole diameters (33 mm, 63 mm) for a total of 4 membrane parameter combinations. Testing was repeated for two membrane samples labeled with alphabetical identifiers at each combination and with 5 indentations at each pressure increment. Stiffness values were then extracted from the force-displacement curve.

The system's capability to simulate physiological stiffness was defined by repeated indentation testing of membranes (n=3) using membrane and inflation parameters associated with measured stiffness near 0.33 and 0.81 N/mm. Because of a high degree of linearity and predictability in measured stiffness versus pressure, a minimum of three indentation tests could be used to define the system's upper and lower limits. Therefore, indentation testing with the BOSE was repeated on a single layer membrane constrained by the 33 mm diameter plate with pressures ranging from 0.7 to

0.9 psi to define the acceptable lower limit. Similarly, a double layer membrane constrained by the 63 mm diameter plate was probed within the range of 1.3 to 1.5 psi to define the acceptable upper limit. Stiffness values were again extrapolated from force-displacement curves. Tissue phantom identifiers A-J and corresponding parameter combinations of membrane layers and constraint diameters are reported in Table 4.1.

Statistical analysis for comparing measured stiffness values to the reported physiological range and for defining acceptable boundaries of the benchtop simulator was completed in three phases:

1. Perform *t* tests to compare mean stiffness measurements of each phantom membrane to 0.33 and 0.81 N/mm across inflation pressures.
2. Perform paired *t* tests to compare the mean of three lower stiffness measurements to 0.33 N/mm.
3. Perform paired *t* tests to compare the mean of three upper stiffness measurements to 0.81 N/mm.

Biaxial Loading of Mesh-Tissue Phantom Composites

Similar to mesh-phantom composite characterization in Chapter 3, a more robust simulation of the *in situ* biaxial loading of abdominal wall tissue during hernia repair surgery also required a relevant reinforcement material to mimic implanted mesh. A preliminary evaluation of the tissue-phantom composite under biaxial load was achieved by overlaying an inflated membrane with knit polypropylene mesh (Prolene Soft, Ethicon, New Jersey, USA) for characterization in terms of stiffness.

Constraint diameter and phantom membrane thickness associated with a mid-range of physiological stiffness was chosen for characterization with mesh reinforcement. A single layer membrane was overlaid with a mesh sample cut to 100 mm by 100 mm and constrained under the larger 63 mm plate (Figure 4.4). The composite was inflated with applied pressure ranging from 0.4 to 1.6 psi at increments of 0.1 psi. At each increment, the mesh-phantom composite was probed by the BOSE and attached spherical indenter 5 times to 10 mm at a rate of 10 mm/s. Testing was repeated on the inflated mesh-phantom composite with the stiffness tool at 0.4, 1.0, and 1.6 psi with no user-load applied during 5 indentations at each pressure increment. Stiffness values were extrapolated from the linear region of each force-displacement curve in the range from 5 to 10 mm of indentation. Paired *t* tests were used to compare stiffness acquired with both measurement instruments at 0.4, 1.0, and 1.6 psi.

Calculated Biaxial Tension of Tissue Phantoms

Under physiological pressure and distension, the tissue phantom membranes and mesh-phantom composite were further characterized in terms of biaxial tension. With a known circumference of each sample limited by the top plate and calculated vertical displacement, the radius of curvature of an inflated membrane was calculated as:

$$R = \frac{a^2+h^2}{2h} \text{ (mm)} \qquad \text{[Equation 2]}$$

where R is the radius of curvature, a is the radius of each sample as limited by the top plate, and h is vertical displacement measured in millimeters (Figure 4.5). Assuming a thin membrane condition where sample thickness is much smaller than its width, the

calculated radius and applied pressure were then used to calculate biaxial tension of the membrane using Laplace's equation:

$$T = \frac{P*R}{2} \quad \text{(N/mm)} \qquad \text{[Equation 3]}$$

where T is biaxial tension and P is the applied pressure (N/mm^2) (Rohrnbauer 2014, Brunon 2011). Using this approach, mechanical characterization was simplified by characterizing loading conditions in terms of membrane tension instead of stress thereby avoiding the need to quantify membrane thickness (Rohrnbauer 2014). Calculation of biaxial tension was completed for all membrane conditions across applied pressures. Linear regression of tension versus pressure was performed for all membranes to evaluate the linearity and predictability of phantom behavior.

4.3 RESULTS

Biaxial Loading of Tissue Phantoms

Tissue phantom membranes were successfully characterized in terms of stiffness from indentation tests with the BOSE ElectroForce system and attached spherical indenter. Stiffness values were extrapolated from the linear region of each force-displacement curve through linear regression in the range from 5 to 10 mm of indentation. All measurement series showed a highly linear relationship between measured stiffness and applied pressure (R^2>0.9).

Most mean stiffness values were statistically similar ($p<0.05$) to the physiological range, with magnitudes greater than 0.33 N/mm and less than 0.81 N/mm. Few combinations of membrane and inflation parameters (e.g. A and H) had mean stiffness

values not within the physiological range ($p>0.05$) thereby exhibiting a wide range of parameters capable of simulating physiological stiffness (Figure 4.6).

When comparing the mean measured stiffness of membranes A, B and I to 0.33 N/mm across pressures from 0.7 to 0.9 psi, the mean stiffness value at 0.9 psi was significantly greater than 0.33 N/mm ($p=0.02$) while those at 0.7 and 0.8 psi were not ($p=0.686$ and $p=0.295$, respectively). Therefore, the lower limit of the system's capability to simulate physiological stiffness near 0.33 N/mm is with a single layer phantom membrane constrained by the 33 mm plate with 0.9 psi of applied pressure. Similarly, when comparing the mean stiffness of membranes G, H, and J to 0.81 N/mm across pressures from 1.3 to 1.5 psi, the mean stiffness value at 1.3 psi was significantly less than 0.81 N/mm ($p=0.036$) while those at 1.4 and 1.5 psi were not ($p=0.206$ and $p=0.869$ respectively). Therefore, the upper limit of the system's capability to simulate physiological stiffness near 0.81 N/mm is with a double layer phantom membrane constrained by the 63 mm plate with 1.3 psi of applied pressure.

Biaxial Loading of Mesh-Tissue Phantom Composites

The mesh-phantom membrane composite was successfully characterized in terms of stiffness from indentation tests with the BOSE ElectroForce system and hand-held stiffness tool. Both measurement series showed a highly linear and predictable relationship ($R^2>0.9$) between stiffness and applied pressure with measured stiffness quickly exceeding the physiological range (Figure 4.7). There was no significant difference ($p=0.684$) between mean stiffness values measured by the BOSE and stiffness

tool at 0.4 psi. Stiffness values measured by both instruments at 1.0 and 1.6 psi were found to be significantly different ($p<0.05$) with a difference of 9.2% and 7.4% respectively (Table 4.2)

Calculated Biaxial Tension of Tissue Phantoms

With known constraint dimensions, applied pressure, and measured vertical displacement, tissue phantom membranes and a mesh-phantom composite membrane were characterized in terms of biaxial tension calculated using Equations 2 and 3. Linear regression of tension versus pressure revealed a highly linear relationship for all membranes ($R^2=0.99$). This was anticipated as vertical displacement increased linearly with applied pressure. Plots of tension versus pressure followed trends much like those of stiffness versus pressure whereas membranes of similar constraint diameter and thickness were calculated to have similar tension (e.g. E and F) (Figure 4.8).

4.4 CONCLUSIONS

The uniaxial system described in Chapter One and Two was limited by boundary conditions of the mesh under tension and by the static stiffness of the underlying phantom. A more robust system was developed to apply biaxial loading to abdominal wall tissue phantom membranes created from standard latex resistance bands. By applying physiologically relevant pressures, phantom membranes were effectively distended and characterized in terms of calculated tension and measured stiffness within the physiological range.

Some variation was seen in stiffness measurements and tension calculations. Several membranes were constrained in their vertical displacement due to limits of the BOSE system; stiffness versus pressure curves of these membranes were therefore cut short. Variations in measurements were most likely due to minor user error in applying consistent pressures across all membranes and in measuring vertical displacement; both of which allowed for some subjective estimation. Ideally, errors would be minimized with more controlled and precise systems of applying pressure and of measuring vertical displacement such as a computer-controlled air pump and imaging of inflated membranes to track apical position.

Measured stiffness of phantom membranes greatly increased and quickly exceeded the physiological range with the addition of mesh. The study described in this chapter could be expanded to include membranes of different materials or composites of materials to obtain an even wider range of simulated physiological conditions. The benchtop simulator may also be applicable for the evaluation of mesh fixation and shrinkage similar to studies conducted by Maurer, et al., in which relevant mesh materials are fixed onto or between membranous materials and inflated to apply a biaxial tension (Maurer 2014). As the composite deflates, a change in mesh dimensions and orientation of fibers and pores can be evaluated.

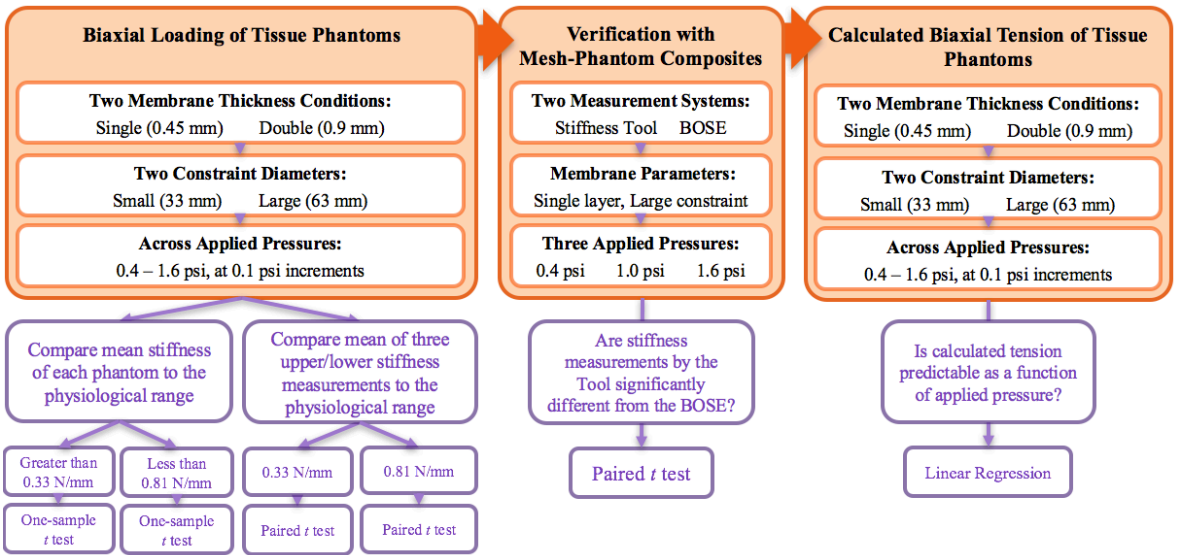

Figure 4.1. Experimental design for the development of a benchtop system to simulate biaxial loading of mesh-phantom composites

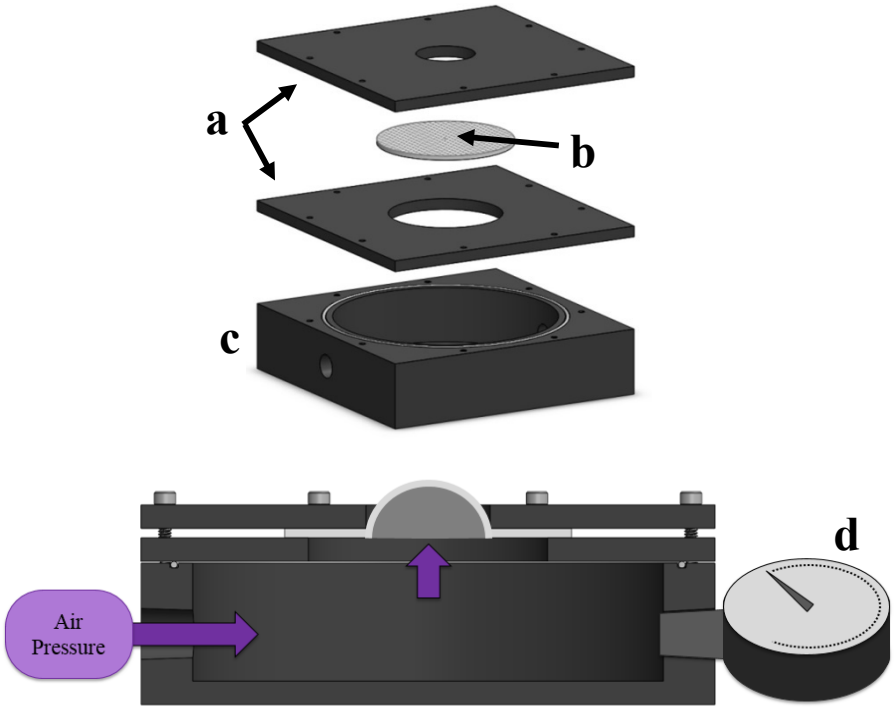

Figure 4.2. Benchtop simulator consists of sample constraint plates (a), tissue phantom membrane (b), pressure chamber (c), and pressure gauge (d)

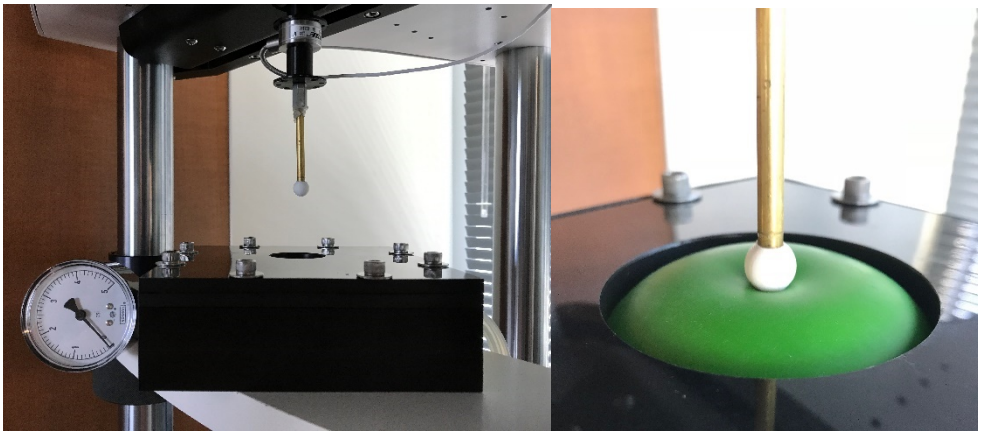

Figure 4.3. Benchtop simulator with phantom membrane centered beneath the BOSE indenter for stiffness characterization

Table 4.1. Phantom membrane identifiers A-J and corresponding parameters

Membrane Thickness / Constraint Diameter	0.45 mm (Single Layer)	0.9 mm (Double Layer)
33 mm	A, B, I	C, D
63 mm	E, F	G, H, J

Figure 4.4. Benchtop simulator test setup for indentation of the mesh-phantom membrane composite with the BOSE ElectroForce system

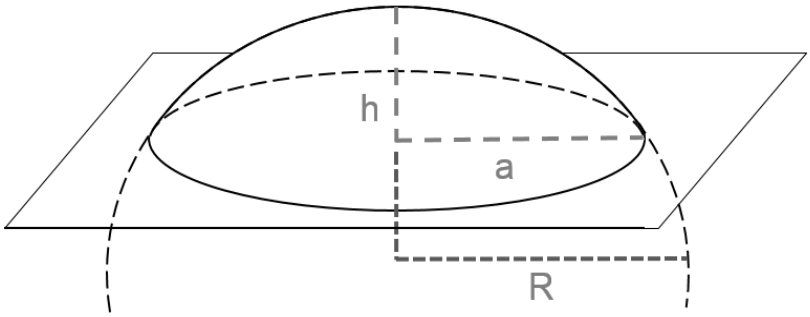

Figure 4.5. Tissue phantom spherical segment geometry to calculate inflated radius of curvature, R

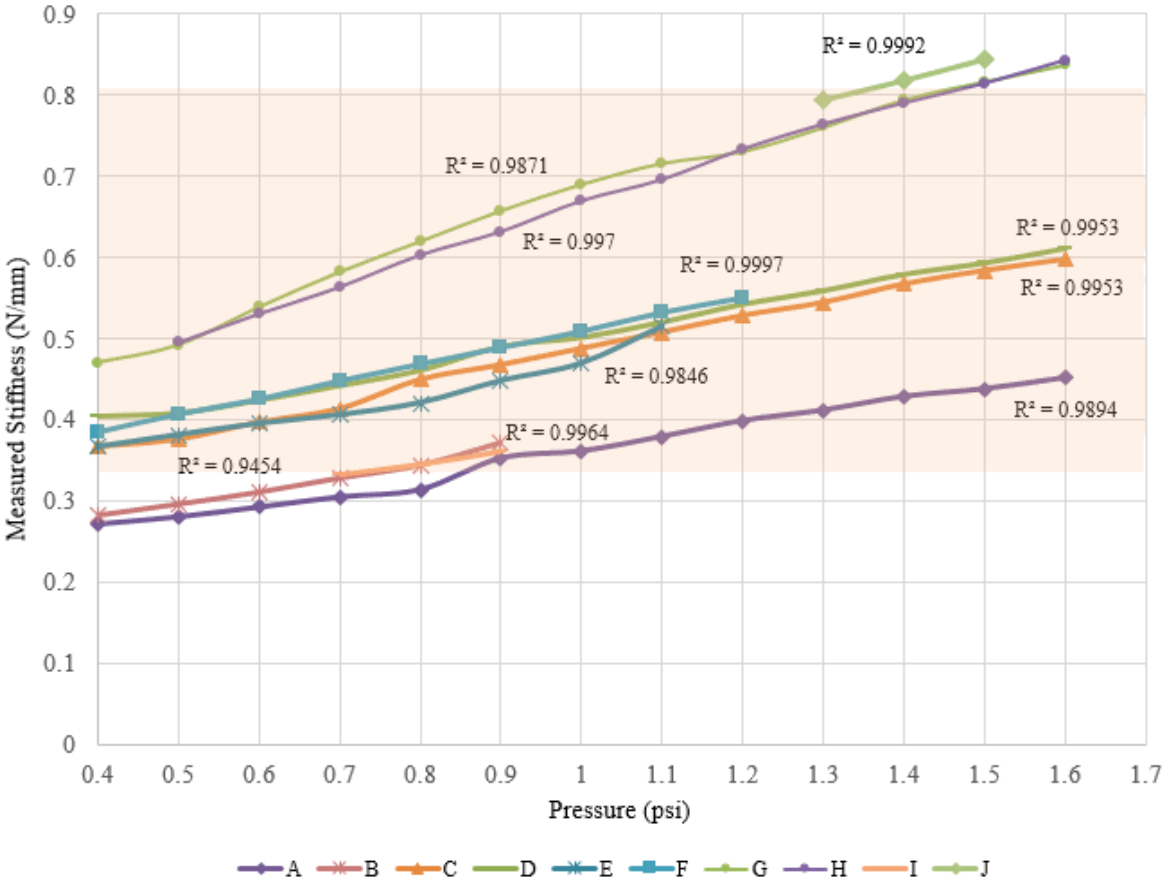

Figure 4.6. Stiffness of phantom membranes measured across increments of applied pressure with R^2 values showing high degree of linearity and physiological stiffness range highlighted

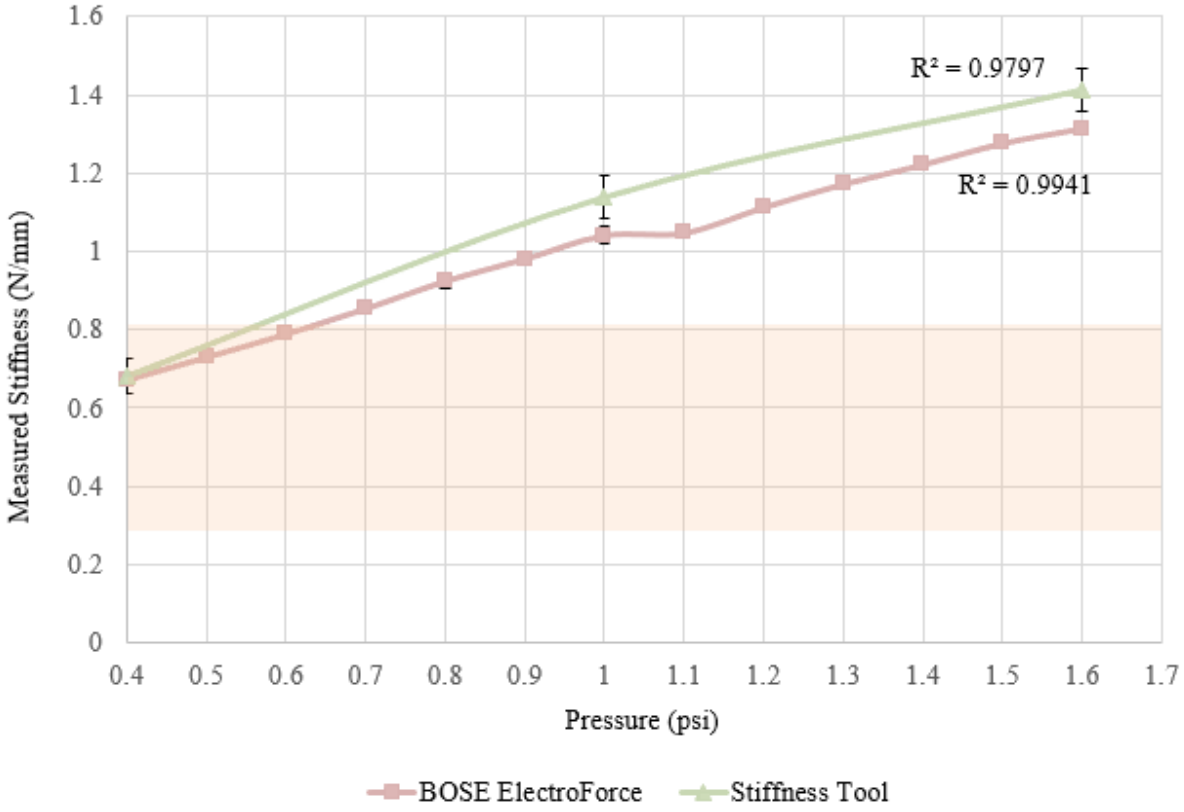

Figure 4.7. Stiffness of the mesh-phantom composite measured by the BOSE and stiffness tool across increments of applied pressure with physiological stiffness range highlighted

Table 4.2. Stiffness of the inflated mesh-phantom composite measured by the BOSE and hand-held stiffness tool (mean ± standard deviation)

Measurement Instrument / **Pressure**	**BOSE ElectroForce**	**Stiffness Tool**
0.4 psi	0.673±0.001	0.681±0.045
1.0 psi	1.04±0.020	1.13±0.055
1.6 psi	1.31±0.004	1.41±0.055

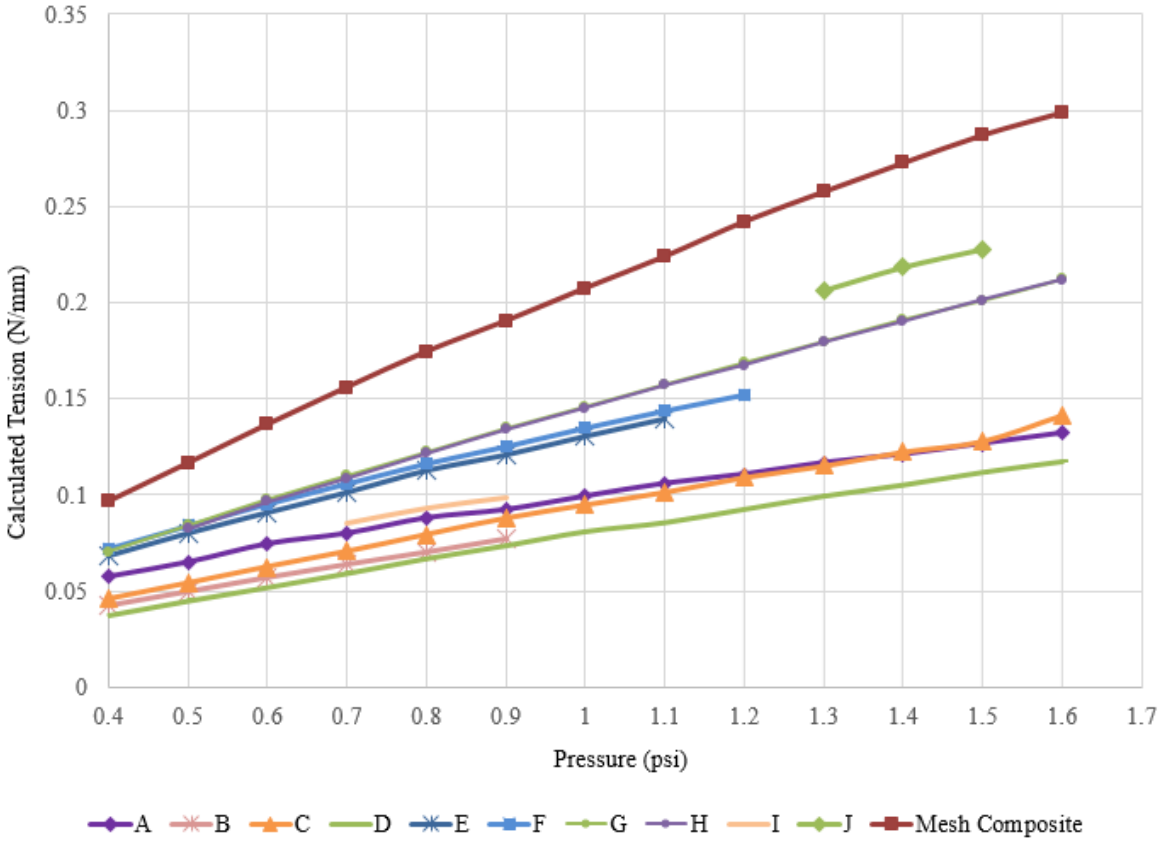

Figure 4.8. Calculated tension of phantom membranes and mesh-phantom composite across increments of applied pressure

CHAPTER FIVE

DISCUSSION

The broad objective of this thesis, to characterize the mechanical behavior of the mesh-tissue composite using abdominal wall tissue phantoms and experimental simulations, was fulfilled through work presented in subsequent chapters. Chapter Two outlined the successful development of a hand-held stiffness tool with instrumentation for mechanical characterization of the abdominal wall. Chapter Three subsequently outlined the effective characterization of mesh-tissue composite stiffness in a uniaxial tension simulator with abdominal wall tissue phantoms and surgical mesh. Finally, Chapter Four presented the successful development of a custom benchtop simulator to mimic abdominal wall distension and provide biaxial loading of mesh-phantom composites.

Development and Application of the Stiffness Tool

Chapter Two presented the development of a hand-held stiffness tool capable of characterizing the abdominal wall with instrumentation to measure load applied to the tool by a user during operation, thereby satisfying Specific Aim 1. The final design of the stiffness tool presented in this thesis was accomplished through iterative design utilizing rapid prototyping and additive manufacturing. Multiple user-load sensors and configurations were considered, all of which had limitations affecting the precision and functionality *in vitro*. Ultimately, the selected load sensor served as the driving factor for design of the removable sheath – a feature which proves useful during cleaning and assembly of the stiffness tool. Additional functional and aesthetic alterations to the tool

were considered secondary to requirements of spherical indentation, stiffness characterization, and user-load measurement.

Verification of the tool was successfully completed against standard benchtop equipment and abdominal wall tissue phantoms characterized in terms of stiffness within the physiological range. Application to swine specimens showed that the tool has potential for use as a clinical instrument for characterizing the abdominal wall *in situ*. The swine specimens tested were collected shortly after surgical procedures, a potential source of variation in their abdominal wall stiffness. They were subject to various incisions and sutures before testing with the stiffness tool began but were only needed for assessing the tool's performance against tissue and not for an exact measure of abdominal wall stiffness. The swine cadaver studies proved useful in verification of the hand-held stiffness tool and in serving as preliminary *in vivo* validation.

The experimental design outlined in Chapter Two was further developed to satisfy Specific Aim 2 for the characterization of mesh-tissue composite stiffness in a uniaxial tension simulator with abdominal wall tissue phantoms and surgical mesh. In Chapter Three, a custom rig was used to apply a range of uniaxial tension to surgically relevant mesh overlaying abdominal wall tissue phantoms. The mesh-tissue composites were characterized with the BOSE ElectroForce benchtop system as well as the hand-held stiffness tool under a range of applied loads. The effects of user-load on stiffness measurements were better defined and effectively minimized using optimization factors corresponding to specific applied loads. This revealed a highly linear relationship from which a simple linear model could be extrapolated and used to correct stiffness values

acquired under a measurable user-load. Initially, it was hypothesized that the effects of user-load on stiffness measurements could be eliminated by simply subtracting the user-load magnitude from indenter load values. However, doing so with a constant would only shift the force-displacement curve without changing the slope. As discovered through this work, the relationship between an applied load and change in stiffness was more complex than initially believed. Thus, user-load measurements may best serve as a means to evaluate the way in which a user is interacting and leaning into the stiffness tool. The methods described in Chapter Two to evaluate user-load effects on stiffness measurement were assumed to be the most intuitive. However, multiple combinations of user interactions with the stiffness tool could reduce or increase measured stiffness in ways that cannot be corrected with current methods. Therefore, continued development of the stiffness tool to further compensate for human error should be considered.

The instrumentation and programming of the final design performed well considering the prototype and hand-held nature of the stiffness tool. With at least 1,200 indentations performed with the tool through this thesis alone, it proved to be robust and promising for long-term service. The lifespan and performance of the tool could be further improved by manufacturing the tool's casing and internal components with high precision parts and more industrial materials as opposed to those readily available for rapid polymer 3D printing. With these improvements, the stiffness tool could be developed commercially as a research and clinical instrument with application to any soft tissue including characterization of internal abdominal organs, external appendages, or

brain tissue by means of non-destructive indentation (Griffin 2016, Su 2009, van Dommelen 2010)

Mesh-Tissue Composite Simulation and Biaxial Loading

Two silicone rubber formulations (ECOFLEX OO-10 and OO-20) were used as tissue phantoms characterized as having stiffness within the theoretical range of the human abdominal wall (0.33 to 0.81 N/mm). A surgically relevant mesh material (Prolene Soft) was chosen to overlay the phantoms and simulate mesh implanted during hernia repair surgery. It should be noted that surgical mesh materials often exhibit a similar slack region to soft tissues, where under low load (a comfort region), fibers shift and extend before reaching high load (safety region) to shield adjacent tissues from excessive strain (Konerding 2012).

Chapter Four expanded the uniaxial mesh-phantom model to fulfill Specific Aim 3 of this thesis: the development of a benchtop simulator capable of mimicking abdominal distension and providing biaxial loading of mesh-phantom composites. Recently developed methods targeting a more standardized approach for characterizing mesh-biomaterials were used as the basis for design of the benchtop simulator. Tissue phantom membranes were selected so that they were thin yet stiff enough to serve as a simulation of abdominal wall tissues. Configuring the inflated membrane under known constraints and biaxial loading conditions produced a range of stiffness values as characterized by non-destructive indentation and revealed a wide range of acceptable parameters to simulate physiological stiffness. Additionally, the inflated membrane was

considered a spherical segment and with measured vertical displacement and known applied pressure, it was characterized in terms of biaxial tension. All measurement series revealed a highly linear and predictable behavior of the phantom membranes which could prove useful when evaluating the behavior of overlaid mesh or composites with more complex materials. While variations seen in stiffness measurements and tension calculations may be due to minimal subjective estimation of applied pressure and vertical displacement, it is worth noting that standardized methods of non-destructive indentation are often subject to variability and several parameters including indenter geometry can lead to varying results (McKee, 2011). With this in mind, the biaxial loading system and prototype stiffness tool were successful in simulating and characterizing the mesh-tissue composite.

APPENDICES

Appendix A

Engineering-Derived Inputs and Outputs

Table A.1. Engineering-derived design inputs and outputs of the stiffness measurement tool prototype

Design Inputs		Design Outputs	
User Need	Design Requirements	Specification	Design Verification
Accurate and precise measurement of user-load	User-Load sensor accurately measures forces within range of interest	Omega load sensor LC8100-200-10 measures > 4 lbf, with less than 15% difference from load applied by Instron	Load sensor calibration to confirm sensitivity within range of interest
	Load sensor fits within the instrument casing	Area within supporting structures of the casing measure maximum 7.1 mm x 25 mm	Casing is printed with dimensions measuring as specified
Load applied to the instrument is transferred to the sensor	A removable sheath can assemble within the tool casing	The removable sheath has an ID > 18 mm & OD < 30 mm	Sheath is printed with dimensions measuring as specified
	A removable sheath and threaded washer fit flush and concentric with the sensor	The removable sheath can thread onto a washer (10 mm length, 10 mm pitch)	Sheath and washer are printed as specified and can thread together
Full functionality of existing sensors	Indenter load sensor accurately measures forces within range of interest	Forsentek FN25-5 load sensor measures forces from 0.5 to 30 N	Load sensor calibration to confirm sensitivity within range of interest
	Indenter displacement sensor accurately measures indenter depth	Optek OPB732WZ LED sensor measures displacements with high resolution up to 10 mm	Displacement sensor calibration to confirm sensitivity within range of interest
	User-load sensor sits concentric with the indenter with minimal interference	User-load sensor has ID > indenter rod (4.75 mm)	Sensor and rod measure as specified and fit concentrically
Effect of user-load on stiffness measurement is minimized	Stiffness measurements are accurate	Stiffness measurements differ by less than 15% from BOSE readings	Measure sample stiffness with both systems, expect less than 15% difference
	Normalized stiffness measurements are accurate	Normal measurements differ by less than 15% from BOSE readings	Calculate stiffness with reduction algorithms, expect less than 15% difference

Appendix B

Engineering Drawings

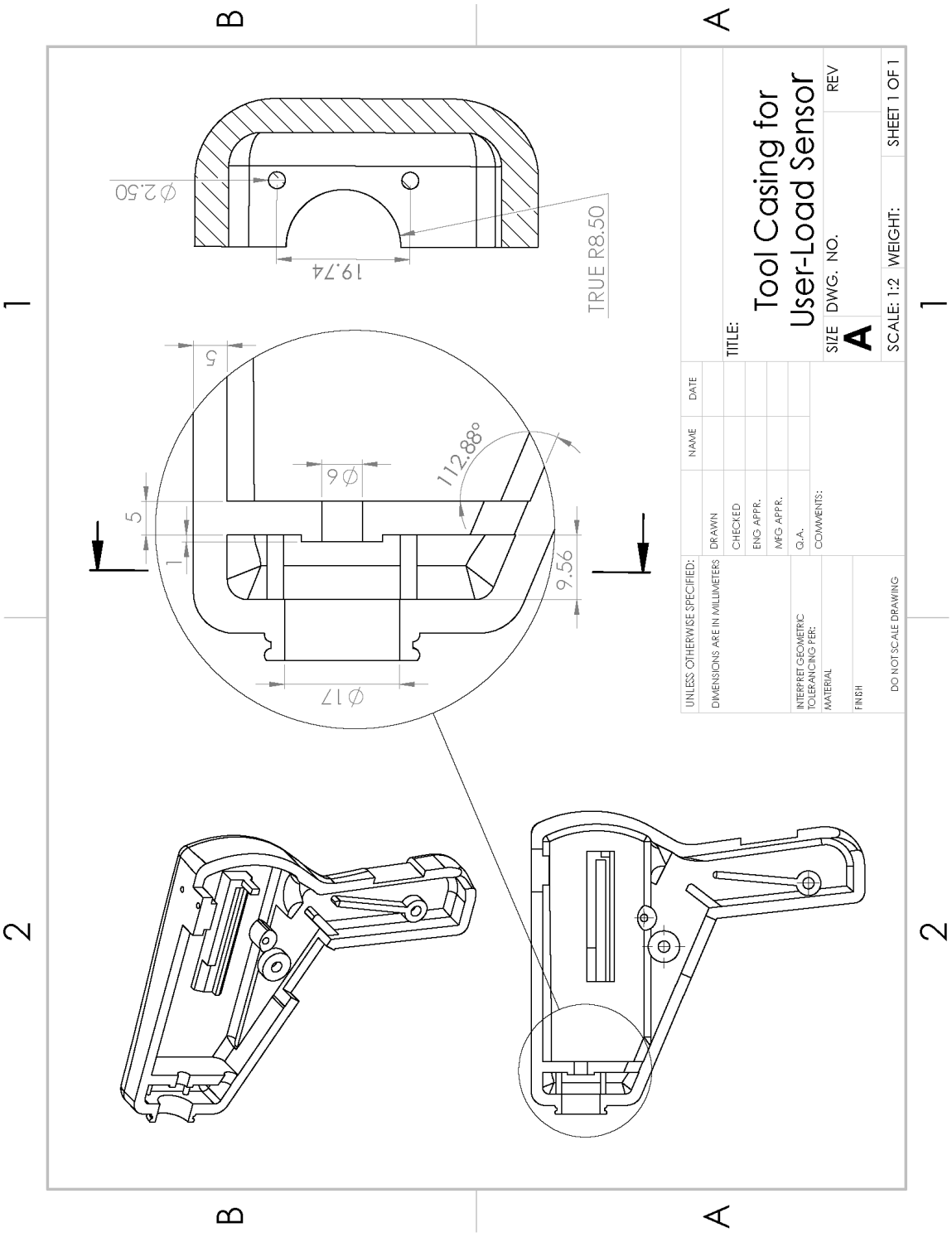

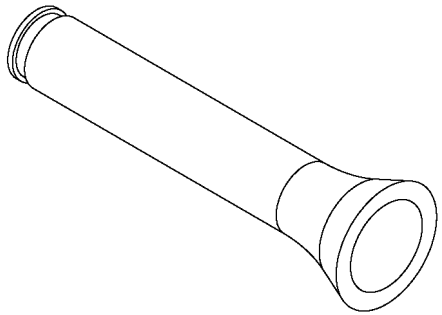

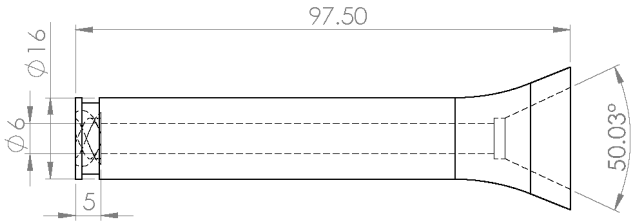

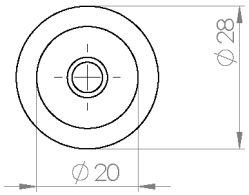

UNLESS OTHERWISE SPECIFIED:		NAME	DATE
DIMENSIONS ARE IN MILLIMETERS	DRAWN		
	CHECKED		
	ENG APPR.		
	MFG APPR.		
INTERPRET GEOMETRIC TOLERANCING PER:	Q.A.		
MATERIAL	COMMENTS:		
FINISH			
DO NOT SCALE DRAWING			

TITLE:

Removable Sheath

SIZE	DWG. NO.	REV
A		

SCALE: 1:1	WEIGHT:	SHEET 1 OF 1

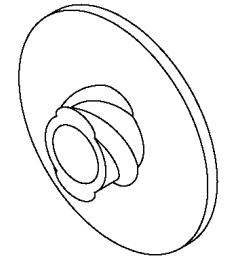

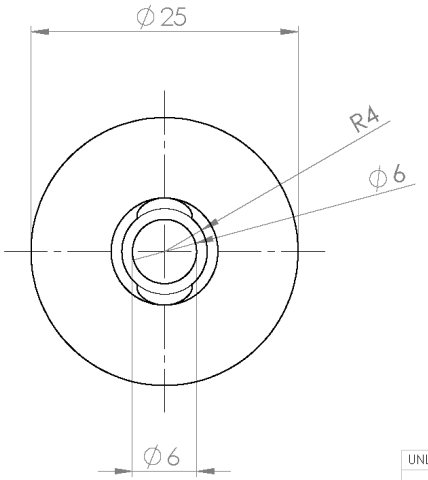

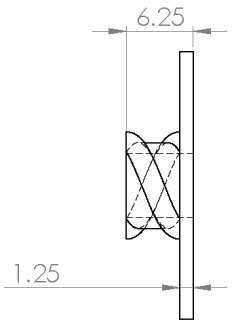

UNLESS OTHERWISE SPECIFIED:		NAME	DATE
DIMENSIONS ARE IN MILLIMETERS	DRAWN		
	CHECKED		
	ENG APPR.		
	MFG APPR.		
INTERPRET GEOMETRIC TOLERANCING PER:	Q.A.		
MATERIAL	COMMENTS:		
FINISH			
DO NOT SCALE DRAWING			

TITLE:

Threaded Washer

SIZE	DWG. NO.	REV
A		

SCALE: 2:1	WEIGHT:	SHEET 1 OF 1

MINIATURE LOW-PROFILE, THROUGH-HOLE LOAD CELLS
1.00 TO 1.25" OD

Compression
0-5 lb to 0-500 lb
0-2.3 kg to 0-227 kg

1 Newton = 0.2248 lb
1 daNewton = 10 Newtons
1 lb = 454 g
1 t = 1000 kg = 2204 lb


LC8125-200-25 shown actual size.

LC8100/LC8125 Series

NIST RoHS
Standard

- **Low Profile**
- **All Stainless Steel Construction**
- **Rugged Industrial Design**

The LC8100 and LC8125 Series donut load cells are an economical solution to applications requiring a through-hole design. With their extremely low-profile and compact design, they are ideal for applications such as clamping forces, bolt loading forces, and other compressive loads. This series, with its all stainless steel construction and environmental protection, has proved reliable in the toughest industrial applications.

SPECIFICATIONS

Output: 2 mV/V nominal
Input: 10 Vdc (15V maximum)
Accuracy: ±1.0% linearity, hysteresis and repeatability combined
Zero Balance: ±2.0% FSO
Operating Temp Range: -54 to 121°C (-65 to 250°F)
Compensated Temp Range: 16 to 71°C (60 to 160°F)
Thermal Effects:
Zero: ±0.009% FSO/°C
Span: ±0.018% rdg/°C
Safe Overload: 150% of capacity
Ultimate Overload: 300% of capacity
Deflection: 0.075 mm (0.003") nominal
Input Resistance: 360 Ω minimum
Output Resistance: 350 ±5 Ω
Construction: 17-4 PH stainless steel
Electrical: 1.5 m (5') 4-conductor shielded cable

Dimensions: mm (inch)

MODEL	OD	H
LC8100	25 (1.00)	7.1 (0.28)
LC8125	32 (1.25)	7.1 (0.28)

WIRE	CONNECTION
GN	+Output
WT	-Output
BK	-Input
RD	+Input

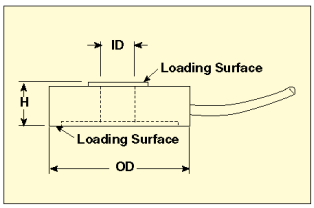

INSIDE DIAMETERS (ID) + = MOST POPULAR X = AVAILABLE							
ID CODE	100	125	188	200	250	312	375
MODEL	0.100"	0.125"	0.188"	0.200"	0.250"	0.312"	0.375"
LC8100	X	X	X	+	X		
LC8125	X	X	X	+	X	+	X

Also available in metric configurations, consult engineering for details.

To Order			
CAPACITY		MODEL NO.	COMPATIBLE METERS**
Model LC8100 with a 1.00" OD and Selectable ID			
5 lb	2.3 kg	LC8100-[*]-5	DP41-S, DP25B-S, DPiS
10 lb	4.5 kg	LC8100-[*]-10	DP41-S, DP25B-S, DPiS
25 lb	11 kg	LC8100-[*]-25	DP41-S, DP25B-S, DPiS
50 lb	23 kg	LC8100-[*]-50	DP41-S, DP25B-S, DPiS
100 lb	45 kg	LC8100-[*]-100	DP41-S, DP25B-S, DPiS
200 lb	91 kg	LC8100-[*]-200	DP41-S, DP25B-S, DPiS
Model LC8125 with a 1.25" OD and Selectable ID			
25 lb	11 kg	LC8125-[*]-25	DP41-S, DP25B-S, DPiS
50 lb	23 kg	LC8125-[*]-50	DP41-S, DP25B-S, DPiS
100 lb	45 kg	LC8125-[*]-100	DP41-S, DP25B-S, DPiS
250 lb	114 kg	LC8125-[*]-250	DP41-S, DP25B-S, DPiS
500 lb	227 kg	LC8125-[*]-500	DP41-S, DP25B-S, DPiS

Comes complete with 5-point NIST-traceable calibration and 59 kΩ shunt data.
*** Visit us online for compatible meters.*
[*] Select ID Code from table above to complete model number.
***Ordering Examples: LC8100-200-200,** 200 lb capacity load cell, 1.00" OD and 0.200" ID.*
***LC8100-125-10,** 10 lb capacity load cell, 1.00" OD and 0.125" ID.*
***LC8125-188-25,** 25 lb capacity load cell, 1.25" OD and 0.188" ID.*
***LC8125-200-500,** 500 lb capacity load cell with 1.25" OD and 0.200" ID.*

F-87

REFERENCES

ASTM International. (2011). D6797 -15: Standard Test Method for Bursting Strength of Fabrics Constant-Rate-of-Extension (CRE) Ball Burst Test. http://doi.org/10.1520/D6797-07R11.2

Brunon, A., Bruyere-Garnier, K., Coret, M. (2011). Characterization of the Nonlinear Behavior and the Failure of Human Liver Capsule Through Inflation Tests. Journal of the Mechanical Behavior of Biomedical Materials, 4(8), 1572-1581. https://doi.org/10.1016/j.jmbbm.2010.12.016

Chhetri, D. K., Zhang, Z., & Neubauer, J. (2011). Measurement of Young's modulus of vocal folds by indentation. Journal of Voice, 25(1), 1–7. http://doi.org/10.1016/j.jvoice.2009.09.005

Cobb, W. S., Peindl, R. M., Zerey, M., Carbonell, A. M., & Heniford, B. T. (2009). Mesh terminology 101. Hernia, 13(1), 1–6. http://doi.org/10.1007/s10029-008-0428-3

Dabbas, N., Adams, K., Pearson, K., & Royle, G. (2011). Frequency of abdominal wall hernias: is classical teaching out of date? JRSM Short Reports, 2(1), 5. http://doi.org/10.1258/shorts.2010.010071

Freytes, D. O., Rundell, A. E., Vande Geest, J., Vorp, D. A., Webster, T. J., & Badylak, S. F. (2005). Analytically derived material properties of multilaminated extracellular matrix devices using the ball-burst test. Biomaterials, 26(27), 5518–5531. http://doi.org/10.1016/j.biomaterials.2005.01.070

Griffin, M., Premakumar, Y., Seifalian, A., Butler, P.E., Szarko, M. (2016). Biomechanical Characterization of Human Soft Tissues Using Indentation and Tensile Testing. J Vis Exp.; (118). doi: 10.3791/54872

Haller, C.M., Buerzle ,W., Brubaker, C.E., Messersmith, P.B., Mazza, E., Ochsenbein-Koelble, N., Zimmermann, R., Ehrbar, M. (2011). Mussel-mimetic Tissue Adhesive for Fetal Membrane Repair: A Standardized ex vivo Evaluation Using Elastomeric Membranes.

Hernandez, J., Harman, M. (2016). Development and Initial Validation of a Surgical Instrument for in situ Mechanical Characterization of Surgical Mesh-Tissue Composites (Thesis). Dept. of Bioengineering, Clemson University, Clemson, SC.

Hodges, P., Gandevia, S. (2000). Changes in Intra-Abdominal Pressure During Postural and Respiratory Activation of the Human Diaphragm. J Appl Physiol, 89: 967-976

Klinge, U., Otto, J., & Mühl, T. (2015). High Structural Stability of Textile Implants Prevents Pore Collapse and Preserves Effective Porosity at Strain. BioMed Research International, 2015.

Konerding, M. A., Chantereau, P., Delventhal, V., Holste, J. L., & Ackermann, M. (2012). Biomechanical and histological evaluation of abdominal wall compliance with intraperitoneal onlay mesh implants in rabbits: A comparison of six different state-of-the-art meshes. Medical Engineering and Physics, 34(7), 806–816. http://doi.org/10.1016/j.medengphy.2011.09.022

Kulacoglu, H. (2011). Current options in inguinal hernia repair in adult patients. Hippokratia, 15(3), 223–231. http://doi.org/10.5152/UCD.2015.2955

Li, J., Liu, H., Althoefer, K., & Seneviratne, L. D. (2012). A stiffness probe based on force and vision sensing for soft tissue diagnosis. Proceedings of the Annual International Conference of the IEEE Engineering in Medicine and Biology Society, EMBS, 1, 944–947. http://doi.org/10.1109/EMBC.2012.6346088

Maurer, M.M., Rohrnbauer, B., Feola, A., Deprest, J., Mazza, E. (2014). Mechanical Biocompatibility of Prosthetic Meshes: A Comprehensive Protocol for Mechanical Characterization. Journal of the Mechanical Behavior of Biomedical Materials, 40, 42-58. http://doi.org/10.1016/j.jmbbm.2014.08.005.

McKee, C. T., Last, J. a, Russell, P., Murphy, C. J. (2011). Indentation versus tensile measurements of Young's modulus for soft biological tissues. Tissue Engineering. Part B, Reviews, 17(3), 155–164. http://doi.org/10.1089/ten.teb.2010.0520

Mitchell, M. R., Link, R. E., Mix, W., Giacomin, J. (2011). Standardized Polymer Durometry. Journal of Testing and Evaluation, 39(4), 103205. http://doi.org/10.1520/JTE103205

Muysoms, F., Campanelli, G., Champault, G. G., DeBeaux, A. C., Dietz, U. A., Jeekel, J., Miserez, M. (2012). EuraHS: The Development of an international online platform for registration and outcome measurement of ventral abdominal wall Hernia repair. Hernia, 16(3), 239–250. http://doi.org/10.1007/s10029-012-0912-7

Ottensmeyer, M. P. (2001). Minimally Invasive Instrument for In Vivo Measurement of Solid Organ Mechanical Impedance, 125.

Pawlak, J. J., & Keller, D. S. (2003). Measurement of the local compressive characteristics of polymeric film and web structures using micro-indentation. Polymer Testing, 22(5), 515–528. http://doi.org/10.1016/S0142-9418(02)00146-0

Poussier, M., Denève, E., Blanc, P., Boulay, E., Bertrand, M., Nedelcu, M., ... Nocca, D. (2013). A review of available prosthetic material for abdominal wall repair. Journal of Visceral Surgery, 150(1), 52–59. http://doi.org/10.1016/j.jviscsurg.2012.10.002

Rohrnbauer, B., Mazza, E. (2014). Mechanical Characterization and Modeling of Prosthetic Meshes (Dissertation). ETH Zurich, Switzerland.

Rutkow, I., & Robbins, A. (1993). Demographic, classificatory, and socioeconomic aspects of hernia repair in the United States. Surg Clin North Am., 73(3), 413–426.

Sahoo, S., DeLozier, K., Erdemir, A., Derwin, K. (2014). Clinically Relevant Mechanical Testing of Hernia Graft Constructs. J Mech Behav Biomed Mater, 41, 177-188. https://doi.org/10.1016/j.jmbbm.2014.10.011

Samur, E., Sedef, M., Basdogan, C., Avtan, L., & Duzgun, O. (2007). A robotic indenter for minimally invasive measurement and characterization of soft tissue response. Medical Image Analysis, 11(4), 361–373. http://doi.org/10.1016/j.media.2007.04.001

Santos, M., Tavares, G., Gasperi, G., Bau, G. (2009). Mechanical Evaluation of the Resistance of Elastic Bands. Rev Bras Fisioter, São Carlos, v. 13, n. 6, p. 521-6.

Song, C., Alijani, A., Frank, T., Hanna, G. B., & Cuschieri, A. (2006a). Mechanical properties of the human abdominal wall measured in vivo during insufflation for laparoscopic surgery. Surgical Endoscopy, 20(6), 987–990. http://doi.org/10.1007/s00464-005-0676-6

Song, C., Alijani, A., Frank, T., Hanna, G., & Cuschieri, A. (2006b). Elasticity of the living abdominal wall in laparoscopic surgery. Journal of Biomechanics, 39(3), 587–591. http://doi.org/10.1016/j.jbiomech.2004.12.019

Su, J., Zou, H., Guo, T. (2009). The Study of Mechanical Properties on Soft Tissue of Human Foreharm In Vivo. International Conference on Bioinformatics and Biomedical Engineering, June 2009. ISSN: 2151-7614

Van Dommelen, J., Van der Sande, T., Hrapko, M., Peters, G. (2010). Mechanical Properties of Brain Tissue by Indentation: Interregional Variation. Journal of the Mechanical Behavior of Biomedical Materials. 3(2). 158-166. https://doi.org/10.1016/j.jmbbm.2009.09.001